NOMAD memo # 2010–01

Precise Measurement of Charm Dimuon Production in Neutrino DIS from the NOMAD Experiment

R. Petti [a] O. Samoylov [b,*]

[a] *Univ. of South Carolina, Columbia SC, USA*

[b] *JINR, Dubna, Russia*

Abstract

We present our new measurement of charm dimuon production in neutrino-iron interactions based upon the full statistics collected by the NOMAD experiment. After background subtraction we observe 15,344 charm dimuon events, providing the largest sample currently available. The analysis exploits the large inclusive charged current sample (about 9 million events after all analysis cuts) to constrain the total systematic uncertainty to $\sim 2\%$. The extraction of charm production parameters is also discussed.

* Corresponding author.
Email address: samoylov@nusun.jinr.ru (O. Samoylov).

1 Introduction

1.1 Strange sea

Parametrization of the strange sea distribution

$$xs(x,Q_0^2) = A_s x^{a_s}(1-x)^{b_s} \tag{1}$$

Strange sea suppression factor

$$\kappa_s(Q^2) = \frac{\int_0^1 x\left[s(x,Q^2)+\bar{s}(x,Q^2)\right]dx}{\int_0^1 x\left[\bar{u}(x,Q^2)+\bar{d}(x,Q^2)\right]dx}, \tag{2}$$

$$\kappa_s(20\text{GeV}^2) = 0.62 \pm 0.04 \pm 0.03(QCD)\ [1].$$

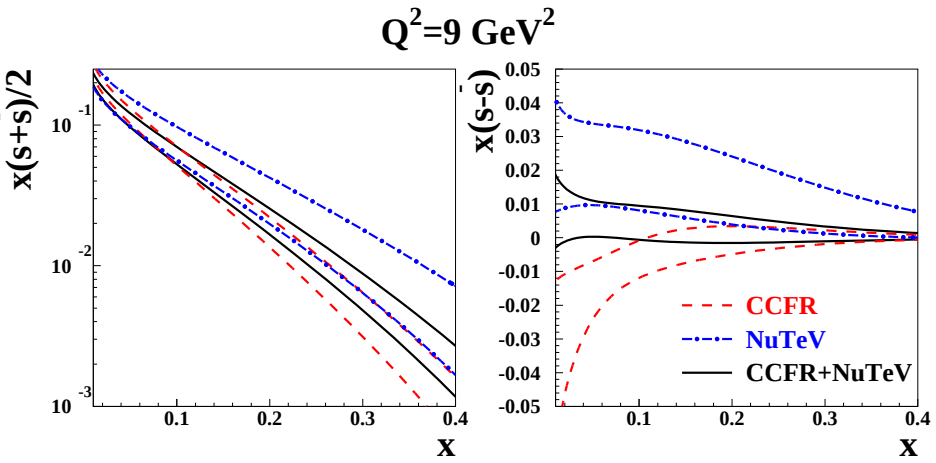

Fig. 1. *Strange sea distributions obtained from a globad PDF fit including the NuTeV and CCFR charm dimuon data [1].*

1.2 Charm dimuon production

Charm Dimuon Fragmentation

$$\frac{d^2\sigma_{\mu\mu}}{dxdydz} = \frac{d^2\sigma_c}{dxdy}\sum_h f_h D_c^h(z) B_c(h \to \mu^+ X), \tag{3}$$

where $h = D^0, D^+, D_s^+, \Lambda_c^+$, $\sum\limits_h f_h = 1$ - type of the charmed hadron,

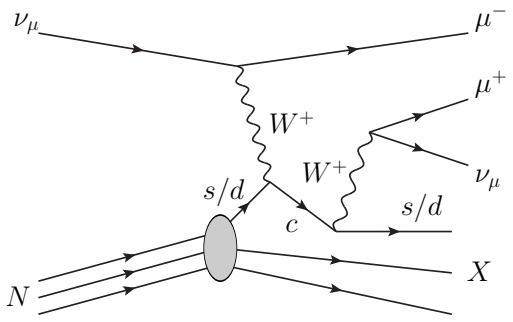

Fig. 2. *Feyman diagram of a ν_μ induced charm dimuon event.*

$$\frac{d^2\sigma_{\mu\mu}(E_\nu > E_\nu^0)}{dxdydz} = \varepsilon_\mu B_\mu \frac{d^2\sigma_c}{dxdy}, \tag{4}$$

where $B_\mu = \sum\limits_h f_h B_c(h \to \mu^+ X)$ - semileptonic branching ratio.

Parametrizations of the Charm quark Fragmentation

$$\begin{aligned} &\text{Peterson:} && D(z,\epsilon) \sim \tfrac{1}{z}\left[1 - \tfrac{1}{z} - \tfrac{\epsilon}{1-z}\right]^{-2} \\ &\text{Collins-Spiller:} && D(z,\epsilon) \sim \left[\tfrac{1-z}{z} - \epsilon\tfrac{2-z}{1-z}\right](1+z)^2\left[1 - \tfrac{1}{z} - \tfrac{\epsilon}{1-z}\right]^{-2} \end{aligned} \tag{5}$$

Physics potential of the Charm Dimuon

- Mass of the charm m_c
- CKM matrix elements V_{cd}, V_{cs} - fixed
- Semi-leptonic branching ratio $B_\mu(E_\nu)$
- Parameter of Charm fragmentation ϵ
- Strange sea distribution $xs(x)$, $x\bar{s}(x)$
- Strange sea asymmetry $x\,(s(x) - \bar{s}(x))$

2 Experimental review

	Exp.	Publ.	Stat. ($N_{\mu\mu}$)	E_ν (GeV)
$\underline{\nu N}$				
	CDHS [2]	Jun 1982	9,922	30-250 (20)
	CHARM II [3]	Oct 1999	3,100	35-290 (24)
	NOMAD [4]	Jul 2000	2,714	14-300 (27)
	NuTeV [5]	Feb 2001	5,102	20-400 (157.8)
	CCFR [6,5]	Feb 2001	5,030	30-600 (150)
	CHORUS [7]	Apr 2008	8,910	15-240 (27)
	NOMAD	2010	15,344	6-300 (27)
$\underline{\bar{\nu} N}$				
	CDHS [2]	Jun 1982	2,123	30-250
	CHARM II [3]	Oct 1999	700	35-290
	NuTeV [5]	Feb 2001	1,458	20-400
	CCFR [6,5]	Feb 2001	1,060	30-600
	CHORUS [7]	Apr 2008	430	10-240

Table 1
Summary of existing measurements of charm dimuon production in neutrino and anti-neutrino interactions. The NOMAD analysis described in this paper has the largest statistics and the lowest energy thresold.

E531 [8] + CHORUS [9]	$E_\nu > 5$GeV	$E_\nu > 30$GeV
B_μ (%)	7.94 ± 0.38	8.78 ± 0.50

Table 2
Inclusive semileptonic branching ratio B_μ obtined from the E531 and CHORUS emulsion experiments [1].

3 Data selection

3.1 The front calorimeter

The front calorimeter (FCAL) in NOMAD consists of 23 iron plates which are 4.9 cm thick and separated by 1.8 cm gaps. Twenty out of the 22 gaps are instrumented with long scintillators which are read out on both ends by 3 in photomultipliers. The dimensions of the scintillators are $175 \times 18.5 \times 0.6$ cm^3. To achieve optimal light collection and a reasonable number of electronic channels five consecutive scintillators along the beam axis are ganged together by means of twisted light guides and form a module. Ten such modules are placed above each other and form a stack. Along the beam axis are four stacks. The area of the FCAL "seen" by the neutrino beam is 175×190 cm^2. The detector has a depth of about five nuclear interaction lengths and a total mass of about 17.7 tons. Figure 3 shows a sketch of the FCAL detector.

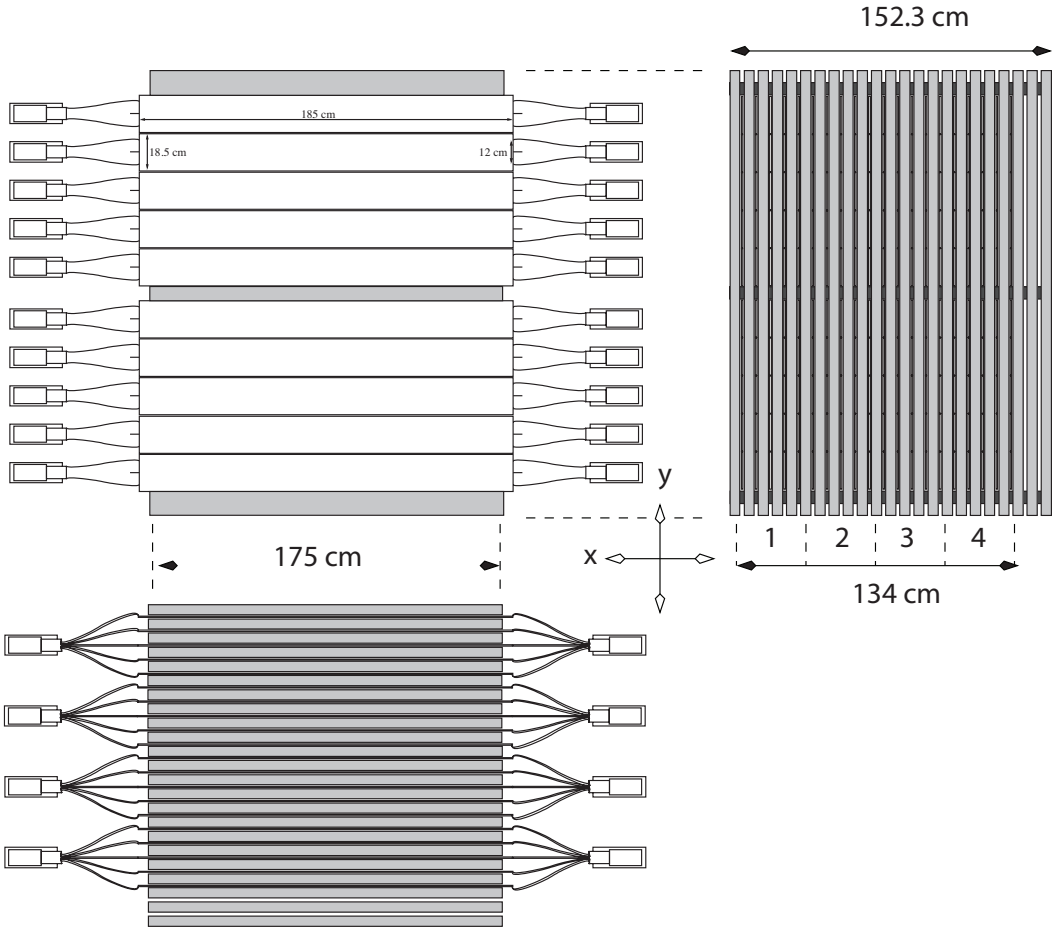

Fig. 3. *Sketch of the FCAL in NOMAD: front view along the beam direction (top left); side view from the right (top right); top view (bottom).*

3.2 Trigger efficiency

The main trigger selection used for the analysis requires an energy deposition of at least 3.15 m.i.p. in the FCAL (FCAL trigger). Through-going muons are vetoed by the V_8 veto scintillator plane: $\bar{V}_8 \times FCAL$. The live time is $90 \pm 3\%$.

A second independent trigger selection with lower thresold is used to measure the FCAL trigger efficiency from data (FCAL$\prime$ trigger). For this trigger an energy deposition of at least 1.2 m.i.p. in the FCAL is requested, in addition to the coincidence with a signal from the scintillator triggers in the TRT region: $\bar{V}_8 \times T_1 \times T_2 \times FCAL'$. The live time is $90 \pm 3\%$.

We measure the efficiency of the FCAL trigger directly from data in the following way:

$$\epsilon_{FCAL} = \frac{N^{DATA}_{FCAL\&FCAL'}}{N^{DATA}_{FCAL'}} \tag{6}$$

We determine the FCAL trigger efficiency separately for each of the 4 stacks and each of the 4 years of data taking, for a total of 16 histograms. Each of those histograms is fitted with the following empirical function:

$$\epsilon_{FCAL}(E) = \frac{p_0}{2}\left[1 + \tanh\left(p_1 + \frac{1}{p_2}\frac{5E^{p_3}}{E + p_4}\right)\right] \tag{7}$$

We calculate the effective trigger efficiency for each stack by averaging over the different years of data taking, weighted by the corresponding numbers of ν_μ CC events identified in the data:

$$\epsilon^{stack}_{FCAL} = \sum_{y=95,96,97,98} \frac{N^{DATA}_{y,stack}}{N^{DATA}_{stack}} \epsilon^{y,stack}_{FCAL} \tag{8}$$

Finally, we implement the resulting FCAL trigger efficiency into our Monte Carlo simulation.

3.2.1 Saturation

The MC simulation does not include the effect of the saturation of the readout electronics which resulted in a reduced value of the ADC counts observed in the data at high energies.

In order to take into account the saturation effect we apply a correction function to the ADC response of each individual FCAL module according to the

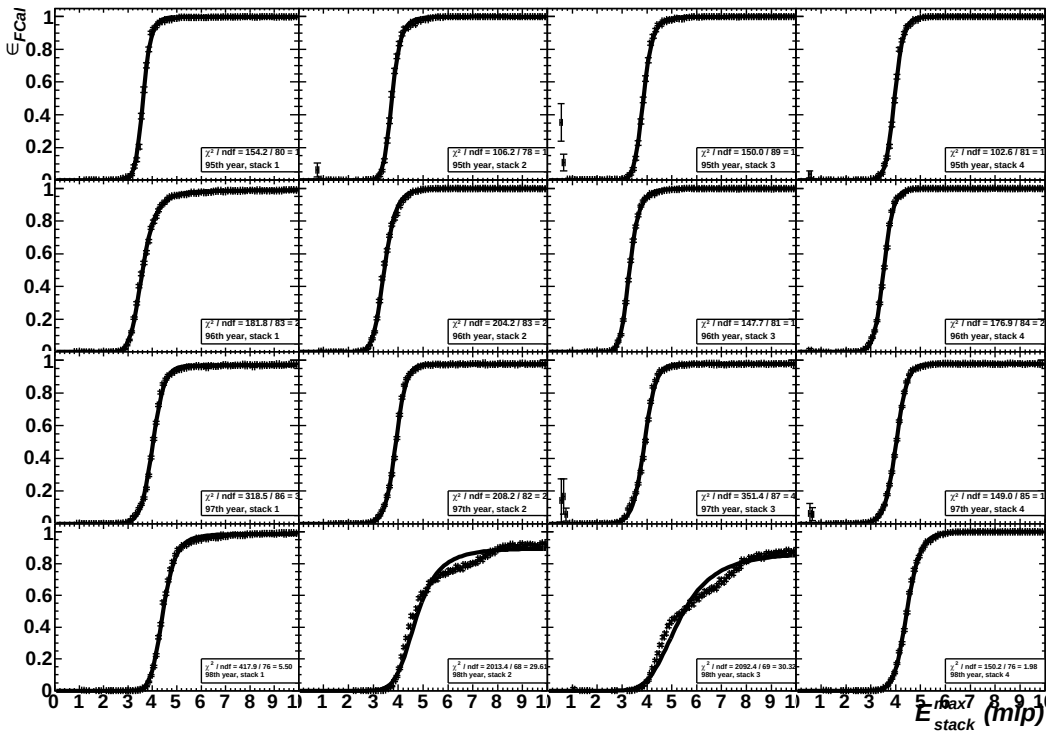

Fig. 4. *FCAL trigger efficiency for each stack (columns) and each year (rows) of data taking.*

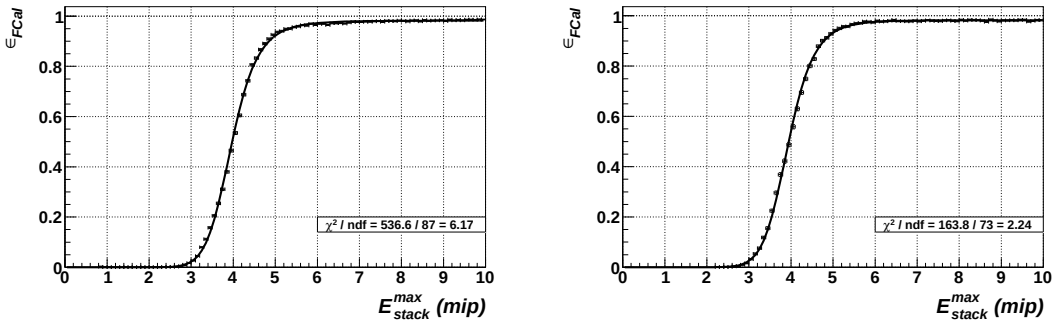

Fig. 5. *FCAL trigger efficiency for the first stack in DATA (left) and MC (right) integrated over the entire data taking period.*

following equation:

$$\mathrm{ADC} = s \cdot \begin{cases} \mathrm{ADC}, & \mathrm{ADC} \leqslant \theta \\ \theta + \dfrac{\mathrm{ADC}-\theta}{\sqrt{1+\left(\dfrac{\mathrm{ADC}-\theta}{\theta}\right)^{p}}}, & \mathrm{ADC} > \theta \end{cases} \tag{9}$$

where s, θ and p are free parameters. For each stack, we compare the total energy measured in the FCAL for ν_μ CC events in data and Monte Carlo (figure 6). We then apply the saturation function described above to each

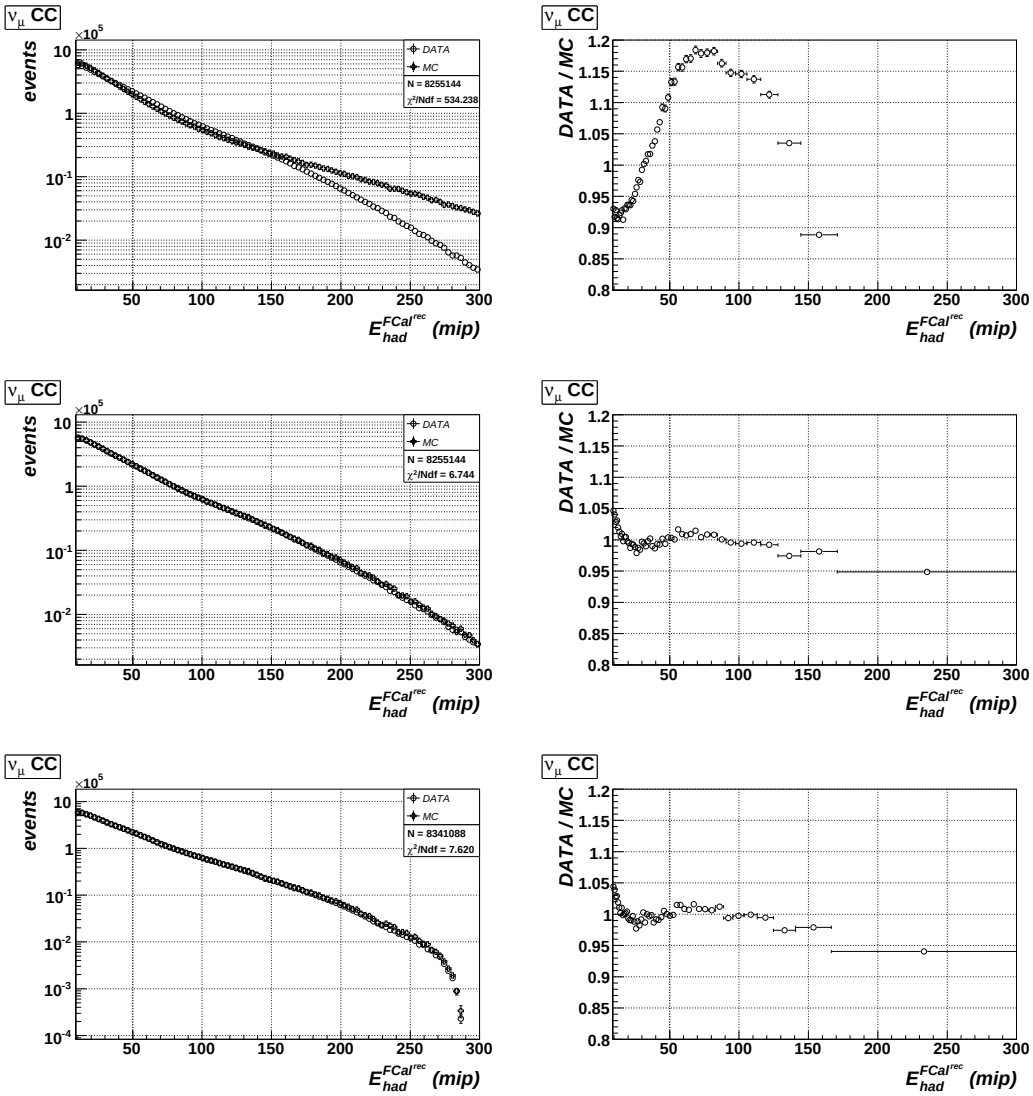

Fig. 6. *Tuning of the saturation correction in FCAL stack by stack: no saturation function applied on MC (top), fitted saturation correction applied to MC (middle), energy calibration applied (bottom, see next subsection)*

FCAL module in the MC and we determine the s, θ and p parameters by minimizing the χ^2 value with respect to data (figure 7). Table 3 summarizes the results for each stack. We note the tuning of the saturation function is an empirical procedure to correct for an effect (saturation of the electronic readout) which is known to affect FCAL data. However, since effectively the MC is tuned to reproduce the hadronic energy deposition of the data, we cannot exclude a priori the saturation function can absorb differences related to the fragmentation. The fragmentation parameters used in the FCAL MC were tuned to reproduce the primary multiplicities measured in DCH data and the comparisons of the inclusive hadron variables in DCH data showed reasonable agreement with the MC simulation.

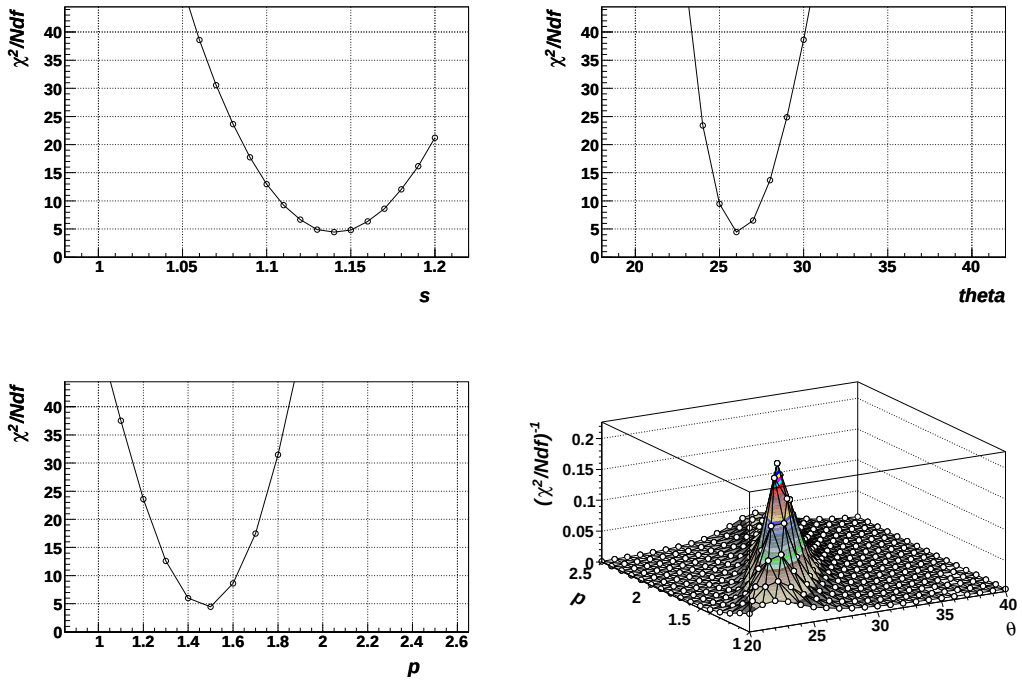

Fig. 7. *Values of χ^2 obtained for each parameter in the saturation function from the fit to data of stack 3 with $s = 1.14$.*

stack 1	s	θ	p	χ^2/Ndf	stack 2	s	θ	p	χ^2/Ndf
	1.06	32.0	1.70	—		1.10	31.0	1.90	—
	1.07	33.0	1.80	—		1.11	32.0	2.00	—
	1.08	34.0	1.90	5.071		1.12	33.0	2.10	2.628
	1.09	35.0	2.00	—		1.13	34.0	2.20	—
	1.10	36.0	2.10	—		1.14	35.0	2.30	—
stack 3	s	θ	p	χ^2/Ndf	stack 4	s	θ	p	χ^2/Ndf
	1.12	24.0	1.30	—		1.03	23.0	1.10	—
	1.13	25.0	1.40	—		1.04	24.0	1.20	—
	1.14	26.0	1.50	4.444		1.05	25.0	1.30	1.229
	1.15	27.0	1.60	—		1.06	26.0	1.40	—
	1.16	28.0	1.70	—		1.07	27.0	1.50	—

Table 3
Best value of χ^2/Ndf for the fit of the saturation function in each stack.

3.2.2 Calibration

The energy deposited in each stack, F^s, is calculated as the sum of the energy depositions of individual FCAL modules (in m.i.p.):

$$F^s = \sum_{i<10} F_i^s, \qquad s = 1, 2, 3, 4. \tag{10}$$

The relative calibration of individual modules in m.i.p. (ADC to m.i.p) is performed by using the energy deposition of high energy muons crossing the FCAL in between the neutrino spills. The muon tracks are reconstructed in the drift chambers and extrapolated back to the FCAL. The absolute energy deposition in GeV is then obtained by dividing the values of F^s by the appropriate mip/GeV conversion factor P_0:

$$E_{had} = \frac{1}{P_0} F_{had} = \frac{1}{P_0} \sum_{s=1}^{4} F^s, \text{ where } P_0 = 2.388 \pm 0.006 \text{ mip/GeV} \qquad (11)$$

where the constant P_0 is obtained from the default MC simulation by comparing the reconstructed to the simulated energy.

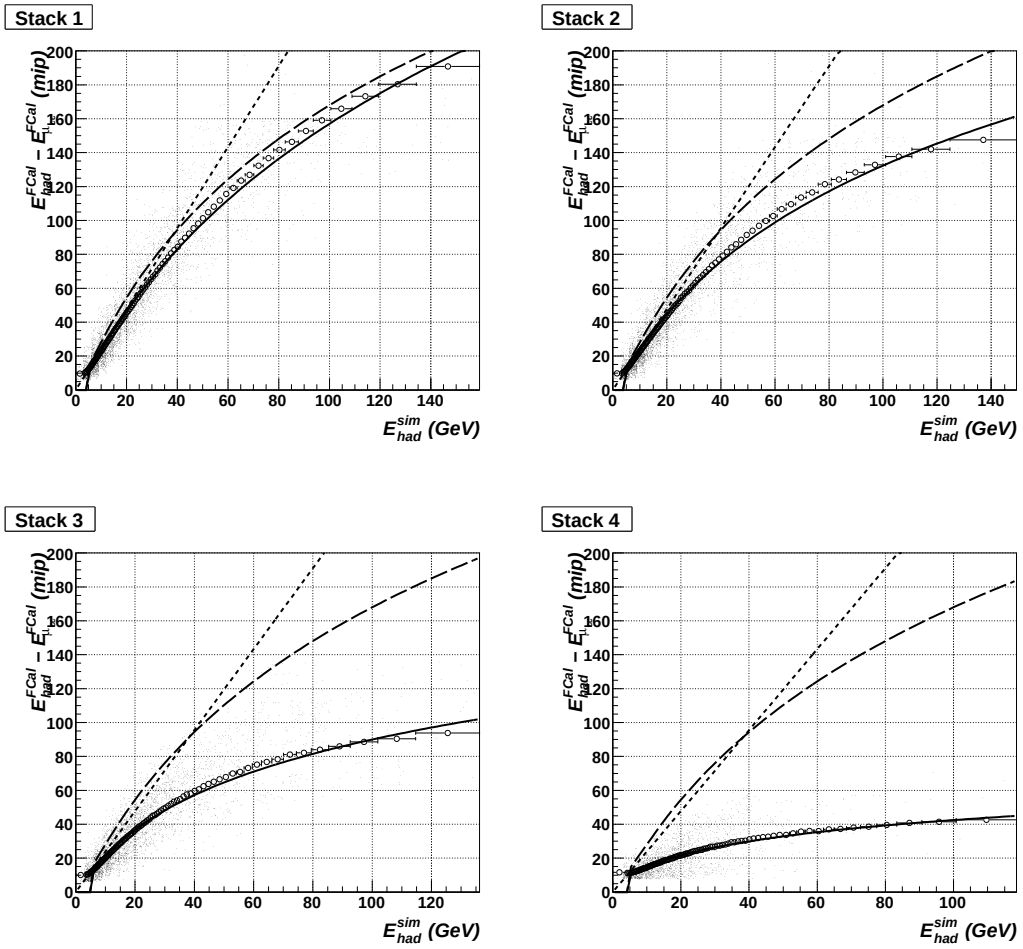

Fig. 8. *Calibration of the FCAL stack by stack from the MC simulation of ν_μ CC interactions. The solid curve is the fitted function according to equation Equation (12), while the dotted curve gives the ideal linear relation of Equation (11). The long–dashed curve is the result of the previous FCAL calibration performed by H. Degaudenzi with different cuts and using only the average of the first three stacks.*

After the smearing of the MC simulation with the saturation function, the

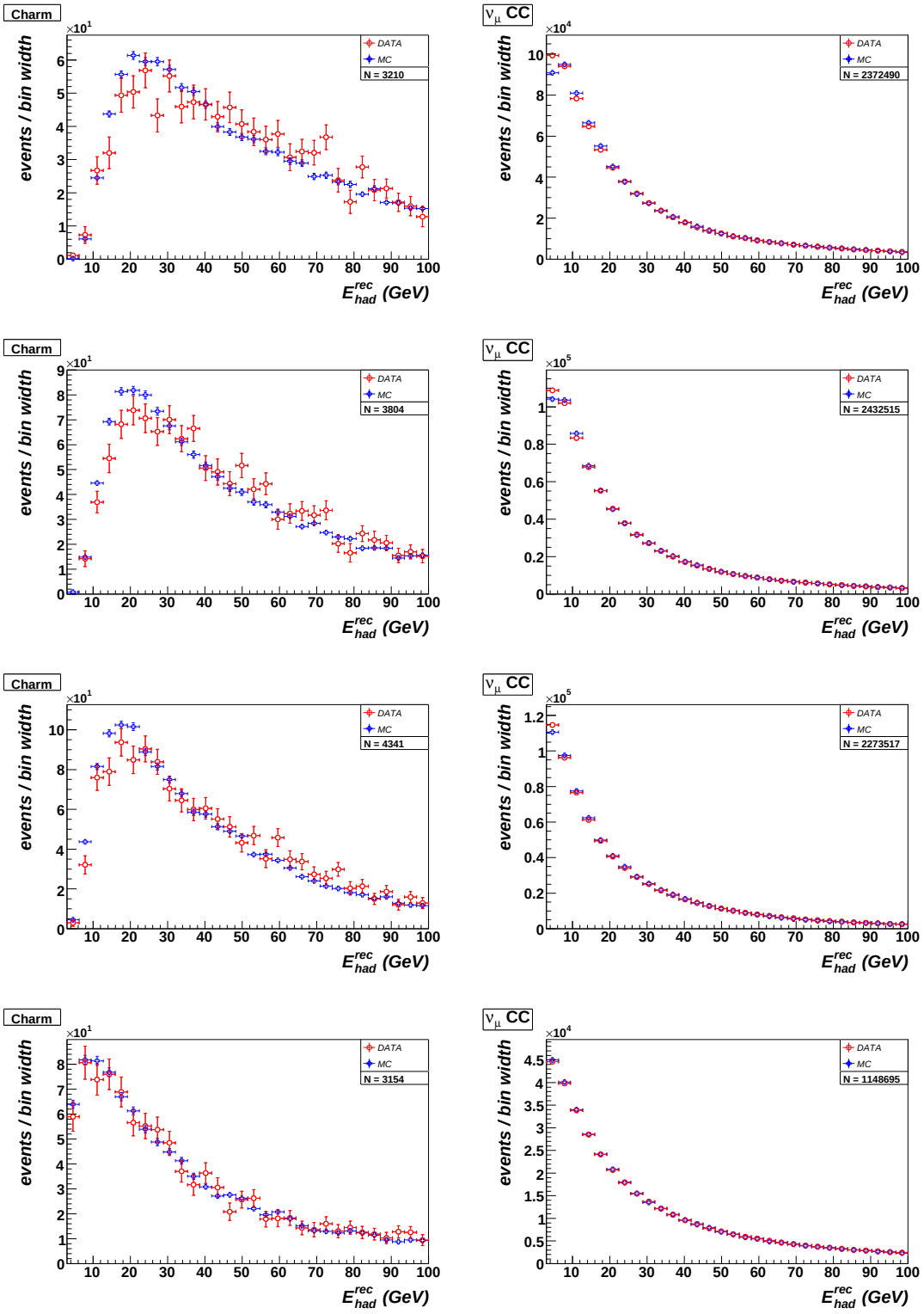

Fig. 9. *Charm (left) and ν_μ CC (right) energy distributions of the hadron shower E_{had}. Each row collects events in one FCAL stack (stack 1 in the top row).*

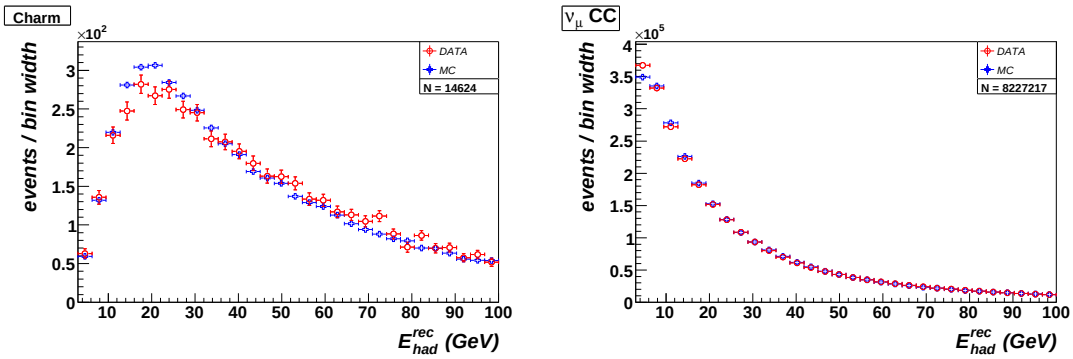

Fig. 10. *Charm (left) and ν_μ CC (right) energy distributions of the hadron shower E_{had} integrated over all FCAL stacks.*

relation between the simulated energy and the energy reconstructed in FCAL is not linear anymore, but follows a more general function $E^{\text{sim}}_{\text{had}} = \mathcal{F}(E^{FCAL}_{\text{had}})$. We extract the inverse function $\mathcal{F}^{-1}$ from the MC simulation by comparing the simulated and reconstructed energy in each stack:

$$\mathcal{F}^{-1} = \begin{cases} P_0 + P_1 E, & E \leqslant P_2 \\ P_0 + P_1 P_2 + P_3 \ln\left[P_4(E - P_2) + 1\right], & E > P_2 \end{cases} \tag{12}$$

where the parameters P_0, P_1, P_2, P_3, P_4 are determined separately for each stack from the Monte Carlo. Figure 9 shows a comparison between data and MC for the final calibrated hadronic energy in each stack for ν_μ CC and charm dimuon events. The corresponding overall distributions, integrated over all stacks, are given in Figure 10.

3.3 Selection cuts

The following cuts are used to select both the ν_μ CC and the dimuon samples:

1 FCAL trigger;
2 Quality cuts: "Bad" runs excluded, number of FCAL modules $n_{mod} < 35$ (40 available in total), total visible energy $E_\nu < 450$ GeV;
3 One phase 2 μ^-;
4 Fiducial volume inside the FCAL: most upstream FCAL stack is one of $1-4$, position of the primary vertex determined from the extrapolation of the muon(s) to the middle z point of the most upstream stack $|x^{PV}_{ext}| < 80$ cm and $|y^{PV}_{ext}| < 90$ cm (see fig. 11);
5* A second phase 2 muon: μ^+ from c-quark production/background or μ^- from background;
6* Time difference between the two muons less then 5 ns to reject backgrounds (see fig. 12);

7* Leading negative muon to reject anti-neutrino background: $P^T_{\mu_{cc}} > P^T_{\mu_c}$;
8* Energy of the hadron shower without the energy of the muon from charm decay ($E_{\rm Had} - E_{\mu_c}$) less than 100 GeV, $E_\nu < 300$ GeV;
9 $x_{b_j} < 1$
10 Energy of the current muon more then 3 GeV (see fig. 13);
11 Energy of the secondary muon more then 3 GeV (see fig. 13) or $E_{had} >$ 3 GeV for CC;
12 $Q^2 > 1$ GeV^2/c^2 (see fig. 14).

where the cuts marked with a * are relevant for the dimuon sample only. All the applied cuts are relatively loose in order to reduce systematic uncertainties. The main goal of the selection is to ensure that the events are well measured in FCAL. We limit our analysis to the region $Q^2 > 1$ GeV^2/c^2 in which we can realiably calculate the cross-sections within the parton model. It must be also noted that the impact of such cut on the charm sample is negligible, due to the intrinsic production threshold. Tables 4 and 5 summarize the effect of the ν_μ CC and dimuon selections on different samples.

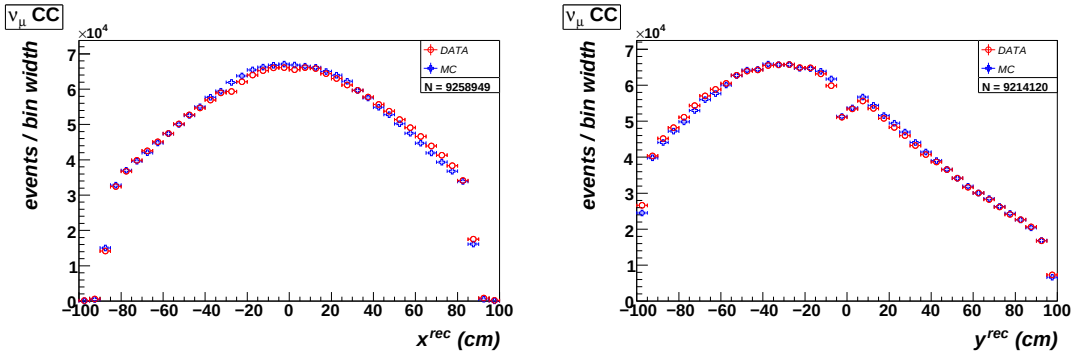

Fig. 11. *Comparison of DATA and MC for fiducial volume inside the FCAL: x-position (left) and y-position (right) of the primary vertex.*

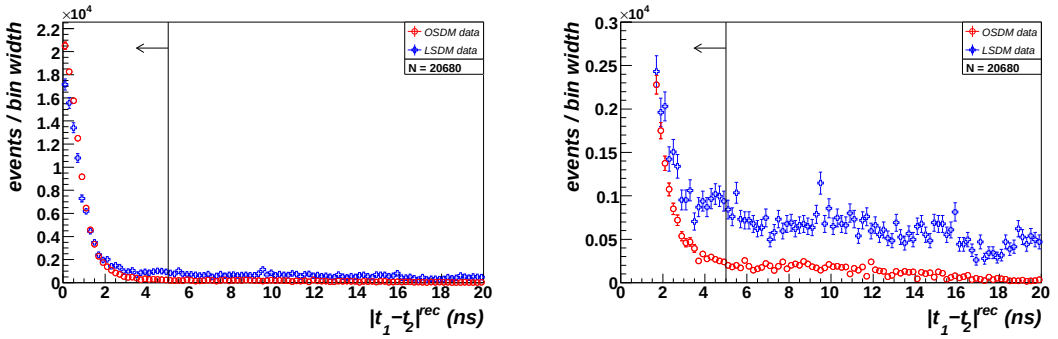

Fig. 12. *Comparison of the time difference between the two muons in OSDM and LSDM data. The histograms are normalized to the same area in the range* $(0-5)$ *ns. The plot on the right is the same as the one on the left, but with a finer vertical scale.*

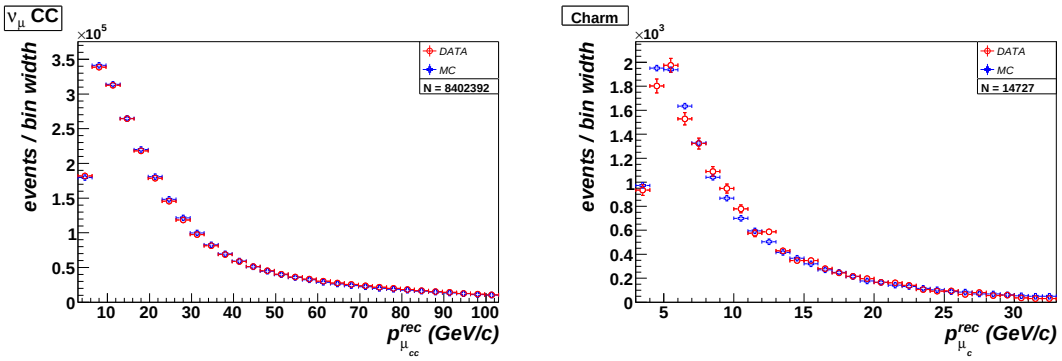

Fig. 13. *Comparison of DATA and MC for energy of the muons: μ^- in ν_μ CC (left) and μ^+ in the Charm (right).*

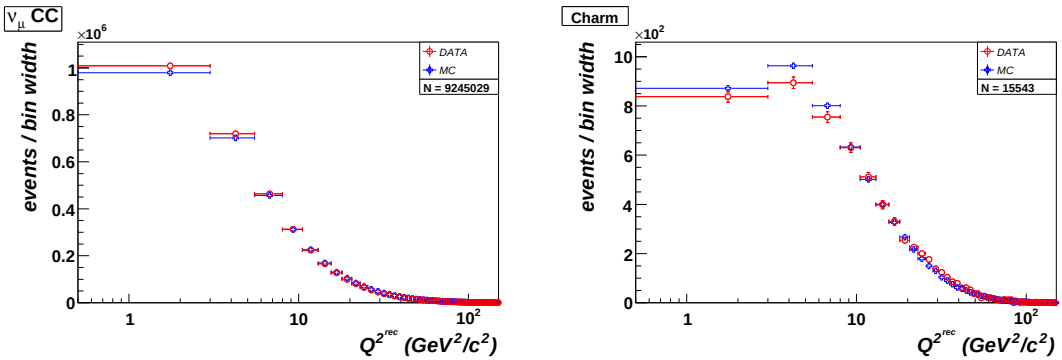

Fig. 14. *Comparison of DATA and MC for Q^2: in ν_μ CC (left) and in the Charm (right).*

3.3.1 Analysis scheme

The analysis measures the ratio of the charm dimuon cross-section to the inclusive CC cross-sectio, as a function of the kinematic variables:

$$\mathcal{R}_{\mu\mu}(x) \equiv \sigma_{\mu\mu}/\sigma_{cc} \simeq N_{\mu\mu}/N_{cc}(x), \text{ where } x = E_\nu, x_{B_j}, \sqrt{\hat{s}} \qquad (13)$$

The ratio $\mathcal{R}_{\mu\mu}$ provides a large cancellation of all systematic uncertainties affecting both the numerator and the denominator.

The ν_μ CC events in the data are well reconstructed and have a negligible background.

The charm dimuon events are determined from the opposite sign dimuons (OSDM) measured in the data after subtracting the background originated from the muonic decay of π^+ and K^+ mesons:

$$N^{\text{DATA}}_{\mu\mu_c} = N^{\text{DATA}}_{\mu\mu^+} - N^{\text{DATA}}_{\mu\mu^+_{bg}} \qquad (14)$$

The background events $N^{\text{DATA}}_{\mu\mu^+_{bg}}$ are estimated from the like sign dimuons (LSDM)

	MC		DATA	DATA/MC
N_{cut} / Type	Rec.	Eff.	Rec.	
simulated	4844438			
weighted	4710173			
eff. corrected	13976553			
1 (trig.)	12143746	—	12451932	1.025
2 (qual.)	12143746	—	12401729	1.021
3 (μ^-)	12126348	—	12298205	1.014
4 (FV)	10639388	76.1%	10757864	1.011
7 (lead. μ^-)	10636157	76.1%	10636157	1.000
8 (E^{up}_{had})	10582711	75.7%	10576596	0.999
9 (x_{B_j})	10359121	74.1%	10381255	1.002
10 ($E_{\mu_{cc}}$)	10354170	74.1%	10376815	1.002
11 ($E^{low}_{\mu_c,had}$)	9730058	69.6%	9615738	0.988
12 (Q^2)	9175383	65.8%	8759065	0.954

Table 4
Event selection for ν_μ CC events in data and MC. The top row shows the raw number of MC events generated in the fiducial volume and used for the normalization of the efficiency. All the other MC numbers have been normalized to data after the fiducial volume and leading muon cuts (cut 7). The ratio of data and normalized MC is also given in the last column.

measured in the data ($\mu^-\mu^-$), multiplied by a scale factor extracted from the Monte Carlo:

$$N^{\rm DATA}_{\mu\mu^+_{bg}} = N^{\rm DATA}_{\mu\mu^-} \cdot \left(N^{\rm MC}_{\mu\mu^+_{bg}} / N^{\rm MC}_{\mu\mu^-} \right) \tag{15}$$

where the scale factor is given by the ratio of opposite sign to like sign dimuon events originated from meson decays (background). In order to reduce the MC statistical uncertainties we generated a total of about 80×10^6 ν_μ CC events fully reconstructed in FCAL. Figure 15 shows the distributions of the LSDM events in FCAL data and MC. The general agreement is satisfactory since we note the LSDM event from MC are never directly used in our analysis. Rather, we only use the *ratio* of OSDM to LSDM background events in MC. This ratio is very sensitive to the details of the fragmentation of the hadronic system, in particular at low momenta. For this reason we cannot rely on the Monte Carlo simulation at the level of precision of a few percent. Instead, we follow a different approach. The background scale is basically determined by the ratio of positively charged to negatively charged mesons inside the hadronic system produced by the fragmentation of partons in DIS events. Therefore, we *measure* this latter ratio as a function of the meson momentum from the

	MC		DATA				DATA/MC	$\sigma_{\mu\mu}/\sigma_{cc}$
N_{cut} / Type	Rec.	Eff.	OSDM	LSDM	Bg.	Charm		
simulated	754684							
weighted	198320							
eff. corrected	69537							4.975
5 (μ^+)	18783	27.0%	30955	33127	—	—	—	—
6 (time)	18671	26.9%	26739	9488	6565	20174	1.080	5.34
7 (lead. μ^-)	18144	26.1%	24642	9488	6366	18276	1.007	5.03
8 (E^{up}_{had})	16287	23.4%	21637	7763	5403	16234	0.997	4.99
9 (x_{B_j})	16180	23.0%	21256	7524	5308	15948	0.985	4.98
10 ($E_{\mu_{cc}}$)	16173	23.0%	21245	7518	5307	15938	0.985	4.97
11 ($E^{low}_{\mu_c,had}$)	16019	22.8%	20949	7324	5269	15680	0.978	5.01
12 (Q^2)	15684	22.5%	20479	7148	5135	15344	0.978	5.15

Table 5

Event selection for dimuon events in data and MC. The top row shows the raw number of MC events generated in the fiducial volume and used for the normalization of the efficiency. All the other MC numbers have been normalized to ν_μ CC data after the fiducial volume and leading muon cuts (cut 7), by taking into account the ratio of charm dimuon cross-section to the inclusive CC cross-section, which are calculated analytically. The number of background events is calculated from the LSDM data multiplied by the scale factor obtained after re-weighting for the h^+/h^- ratio measured in DCH data. The measured ratio of charm dimuons to CC is also given in the last column.

NOMAD data originated in the light Drift Chamber target (DCH). The difference between target nuclei (carbon in DCH vs. iron in FCAL) turns out to be negligible for the inclusive fragmentation variables from a direct comparison between the corresponding MC samples. This comparison is shown in the top left plot of Figure 16. We exclude charged tracks which are either identified as electrons/positrons by the TRD or which have a range consistent with protons. We then subtract the small residual proton/electron/positron contamination by using the MC. Figure 16 shows that the overall contaminations are small even before rejecting identified tracks. The average K/π ratio in neutrino interactions is only about 7% and therefore the uncertainty introduced in the measurement by the different K and π lifetimes is negligible. After measuring the ratio of positively charged to negatively charged mesons from DCH data, we re-weight each positive meson originated from the hadronic system in FCAL events according to the measured ratio ω_{h^+}:

$$W^{\rm MC} = \prod_{h^+} \omega_{h^+} \tag{16}$$

As a result, the entire background estimate for the charm dimuon sample is based upon data themselves, which are used *both* for the LSDM and for the background scale. Figure 16 shows the measured ratio h^+/h^- from the DCH data, as well as a comparison with the corresponding MC simulation. The calibration of the background through the re-weighting procedure is a crucial

step in the analysis and allows a substantial improvement in the description of the charm dimuon data by the Monte Carlo simulation. Without the use of data from the low density DCH target it would have not been possible to lower the energy threshold on the secondary muon to 3 GeV as well as to reduce the systematic uncertainty on the background subtraction. Figure 17 shows the background scale $N^{\rm MC}_{\mu\mu^+_{bg}}/N^{\rm MC}_{\mu\mu^-}$ as a function of the main kinematic variables with and without the re-weighting procedure according to Equation (16). The final background distributions for the OSDM data are given in Figure 18. Table 5 summarizes signal and background events after each selection cut. After all cuts we retain 20,479 OSDM events in the data, out of which 15,344 are genuine charm signal (75%) and 5,135 are background (25%).

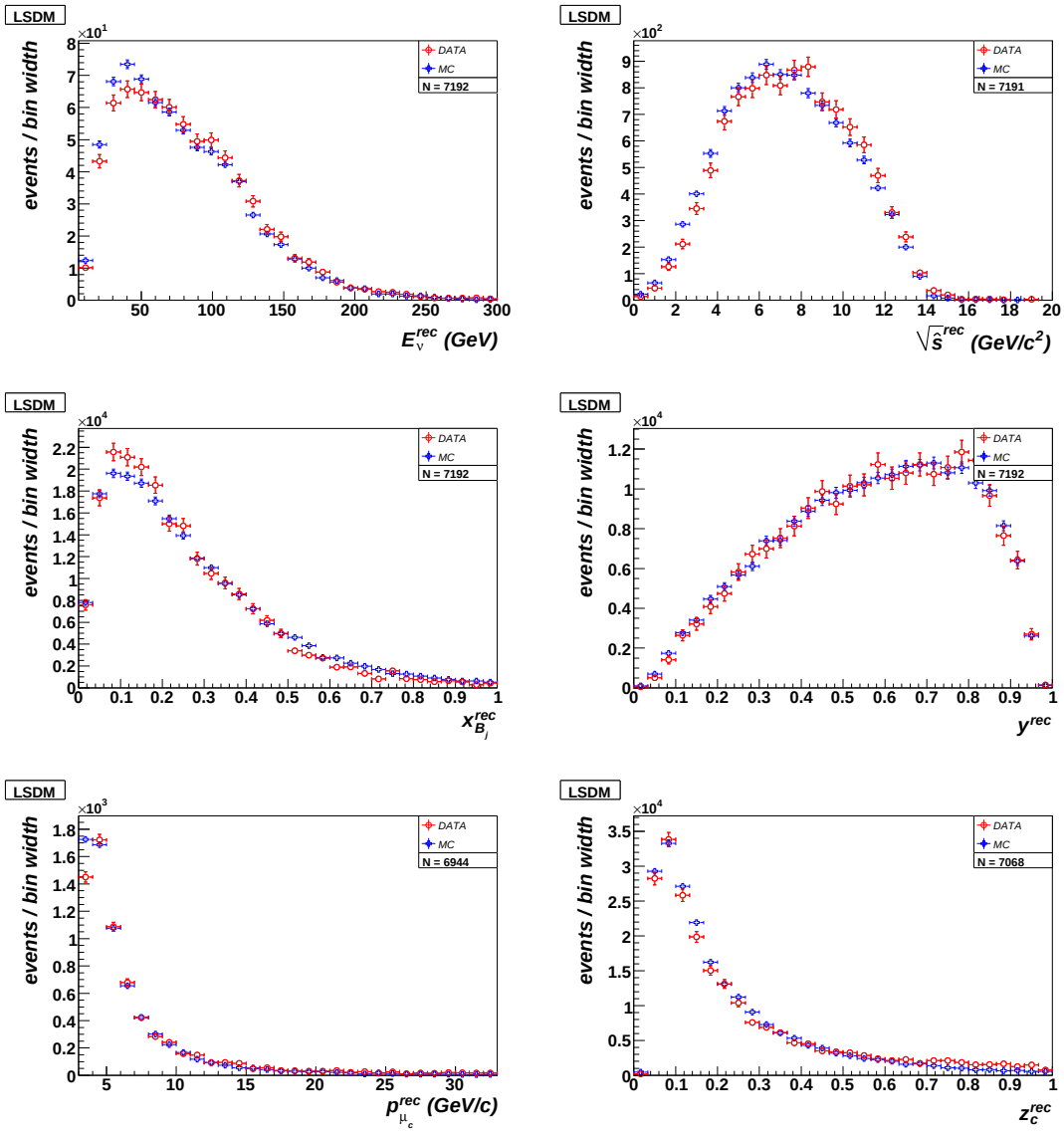

Fig. 15. *Distributions of reconstructed kinematic variables in like-sign dimuon events: visible neutrino energy (top left), center of mass energy $\sqrt{\hat{s}}$ (top right), x-Bjorken (middle left), y-Bjorken (middle right), μ^+ momentum (bottom left), fraction of the energy of the hadron shower carried by the μ^+ (bottom right).. Data are shown as red circles while MC points are shown are blue crosses.*

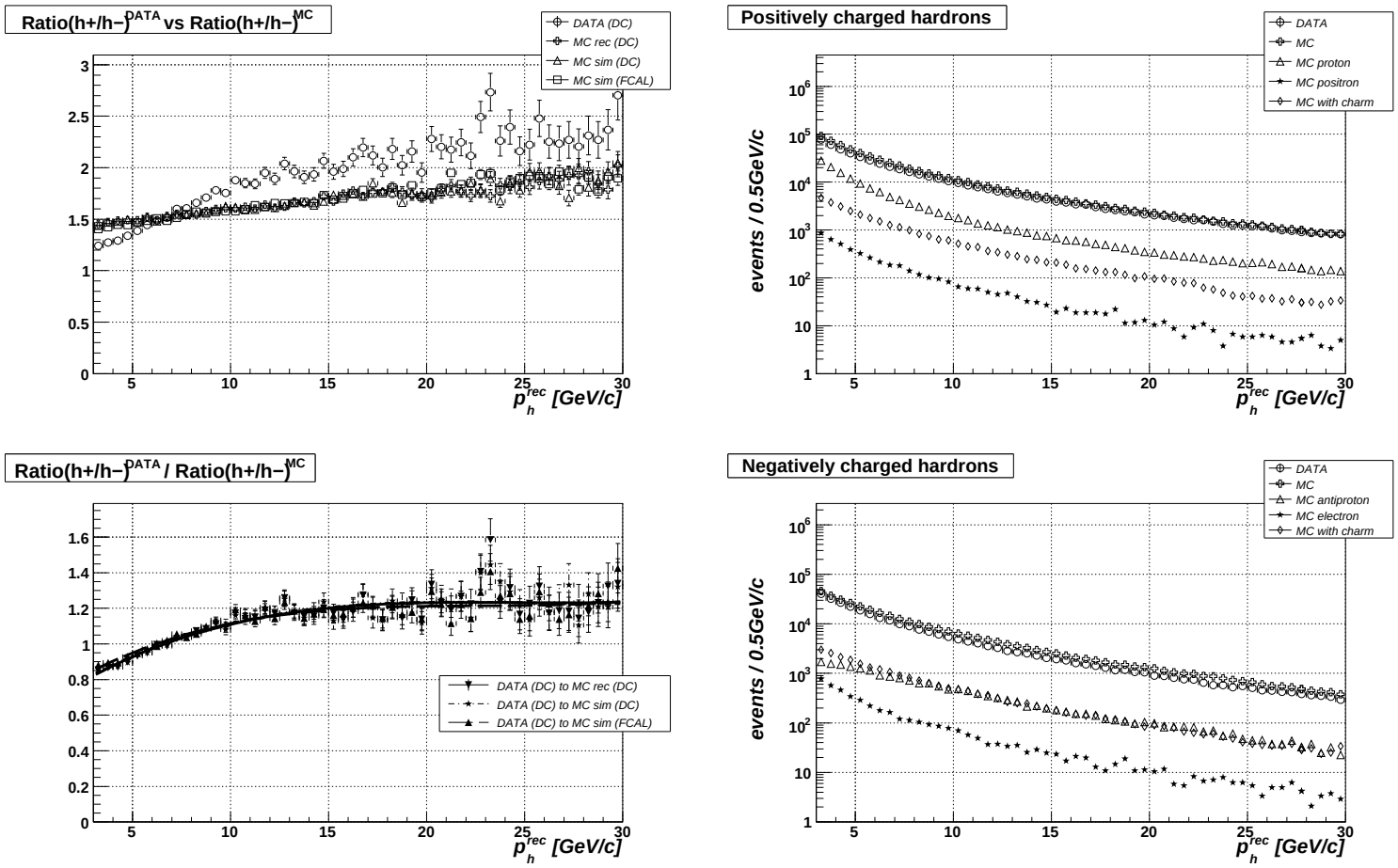

Fig. 16. *Ratio between postively charged and negatively charged mesons h^+/h^- (left) as a function of momentum in DCH data and MC. The bottom left plot shows the double ratio between DCH data and the corresponding MC. The distributions of positively charged (top) and negatively charged (bottom) mesons reconstructed in the DCH target are also given in the right plots.*

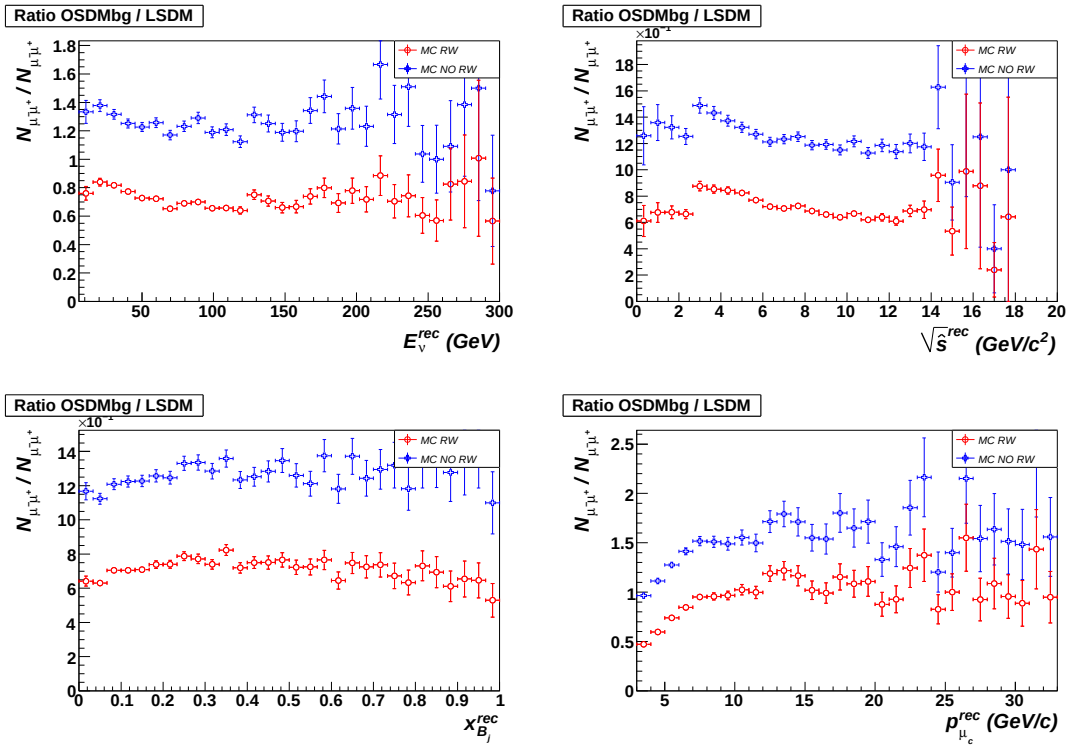

Fig. 17. *Values of the ratio between OSDM background and LSDM from the MC as a function of kinematic variables: visible neutrino energy (top left), center of mass energy $\sqrt{\hat{s}}$ (top right), x-Bjorken (bottom left), μ^+ momentum (bottom right). The blue crosses show the raw MC ratio, while the red circles give the fully calibrated ratio after re-weighting with the h^+/h^- ratio measured in DCH data.*

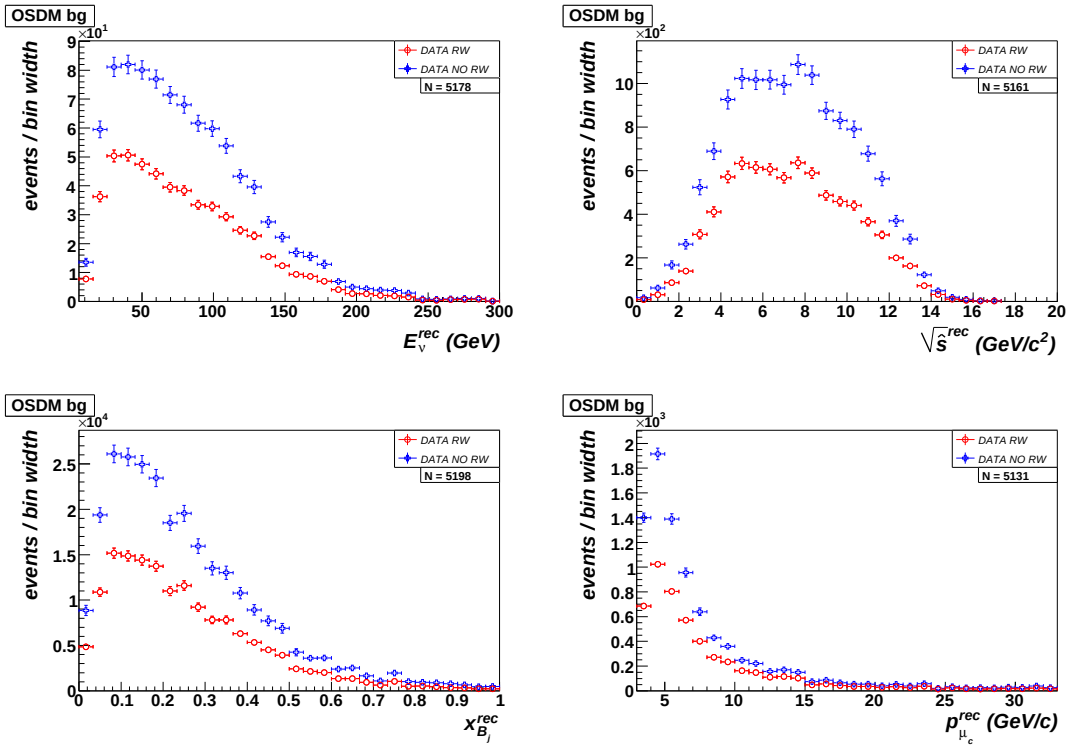

Fig. 18. *Distribution of kinematic variables for the OSDM background in FCAL data: visible neutrino energy (top left), center of mass energy $\sqrt{\hat{s}}$ (top right), x-Bjorken (bottom left), μ^+ momentum (bottom right). The uncalibrated background is shown as blue crosses, while the red circles provide the calibrated background after re-weighting with the h^+/h^- ratio measured in DCH data.*

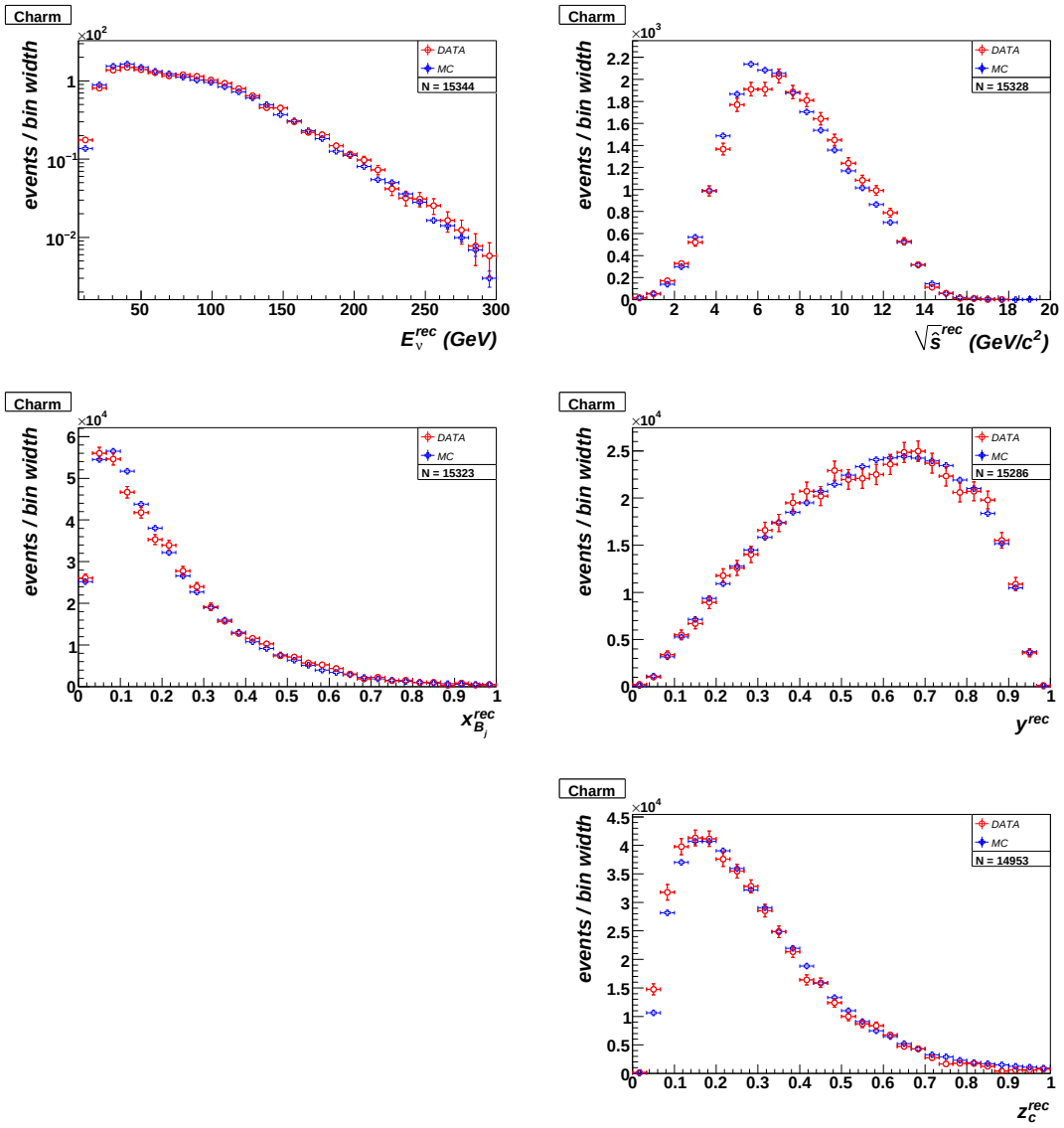

Fig. 19. *Distributions of reconstructed kinematic variables in charm dimuon events: visible neutrino energy (top left), center of mass energy $\sqrt{\hat{s}}$ (top right), x-Bjorken (middle left), y-Bjorken (middle right), fraction of the energy of the hadron shower carried by the μ^+ (bottom right). Data after background subtraction are shown as red circles while MC points are shown are blue crosses.*

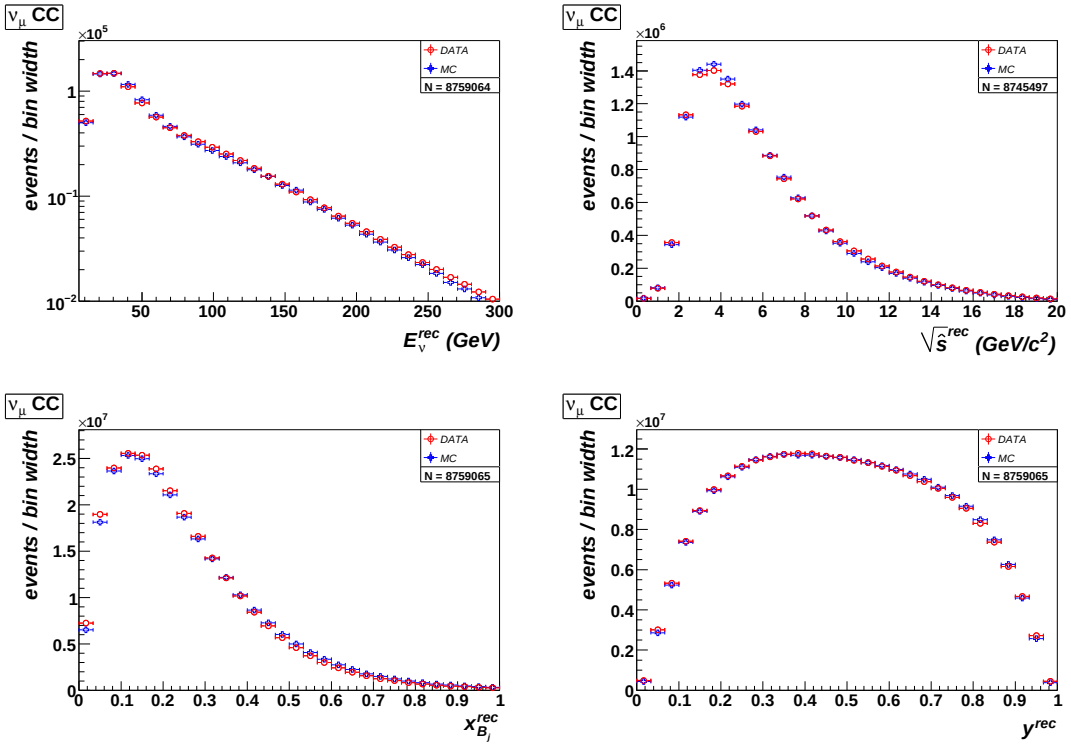

Fig. 20. *Distributions of reconstructed kinematic variables in ν_μ CC events: visible neutrino energy (top left), center of mass energy $\sqrt{\hat{s}}$ (top right), x-Bjorken (bottom left), y-Bjorken (bottom right). Data are shown as red circles while MC points are shown are blue crosses.*

4 Unfolding procedure

The detector smearing and acceptance corrections require an input model for the cross-sections and fragmentation functions. For the inclusive ν_μ CC sample the model is largely independent from the NOMAD data. However, for the charm sample the NOMAD dimuon data are eventually used to determine the charm production parameters, which are, in turn, entering into the experimental acceptance corrections. In our analysis we follow an iterative procedure. First, we use an input model which is fully independent from NOMAD data and we verify its consistency with the NOMAD data. After this step we add NOMAD data to the global PDF fits to improve the precision on the charm production parameters. We then feed back the modified model into the acceptance calculation and iterate until convergence. In the following sections we describe in details the model used and the corrections applied.

4.1 Cross-section weights

The MC events used in the analysis were produced with the default LEPTO cross-sections, which for the DIS are calculated in the LO approximation with GRV94 PDFs. This simulation does not adequately describe the charm production process since it does not include any rescaling mechanism to take into account the large mass of the charm quark. Furthermore, no electroweak, nuclear and high twist corrections are included.

In order to achieve an accurate description of data, we implement a re-weighting procedure for the charm cross-section:

$$\omega_{\mu\mu}(E_\nu, x_{Bj}, y_{Bj}) = \frac{\sigma_{\mu\mu}^{\mathrm{AKP}}(E_\nu, x_{Bj}, y_{Bj})}{\sigma_{\mu\mu}^{\mathrm{LEPTO}}(E_\nu, x_{Bj}, y_{Bj})} \tag{17}$$

where $\sigma_{\mu\mu}^{\mathrm{LEPTO}}$ is the original LEPTO cross-section used to generate the MC events and $\sigma_{\mu\mu}^{\mathrm{AKP}}$ is the new cross-section obtained from an analytical calculation [1,10–14]. The charm cross-section is calculated in the NLO QCD approximation for the heavy quark structure functions, in a factorization scheme with 3 light flavors in the initial state (FFS) [1]. The Target Mass Corrections (TMC) are implemented following the prescription by Georgi and Politzer [15]. The impact of the dynamical High Twist corrections to the charm production is evaluated by applying a simple rescaling for the quark charge to the phenomenological twist-4 terms extracted from the inclusive lepton-nucleon cross-sections [10]. We apply nuclear corrections using the calculations of Refs. [11–13]. This calculation takes into account a number of different effects including the Fermi motion and binding, neutron excess, nuclear shadowing. nuclear

pion excess and the off-shell correction to bound nucleon Structure Functions (SF). The electroweak corrections, including one-loop terms, are calculated according to Ref. [14] within the framework of the parton model. The parameters related to charm production like the mass of the charm quark and the strange sea distribution are fixed to the ones extracted from the global PDF fit including NuTeV and CCFR charm dimuon data [1] at this stage. This allows a consistency check with a calculation fully independent from NOMAD data.

We extract the LEPTO cross-section from the NOMAD MC by simulating 10^9 events with an input flux which is chosen to be inversely proportional to the neutrino energy $\propto 1/E_\nu$.We then bin the events in the (E_ν, x_{Bj}, y_{Bj}) space and smooth the corresponding histograms with an interpolation procedure.

Finally, we apply an additional re-weighting to the charm events to take into account the effect of the charm fragmentation, which is described by the Collins-Spiller function. This function describes the probability for a charmed hadron to carry a given fraction $z = P_L(h_c)/P_L^{\max}$ of the logitudinal momentum and is defined by one free parameter ε. Figure 19 shows a comparison between data and weighted MC for different kinematic variables in charm dimuon events.

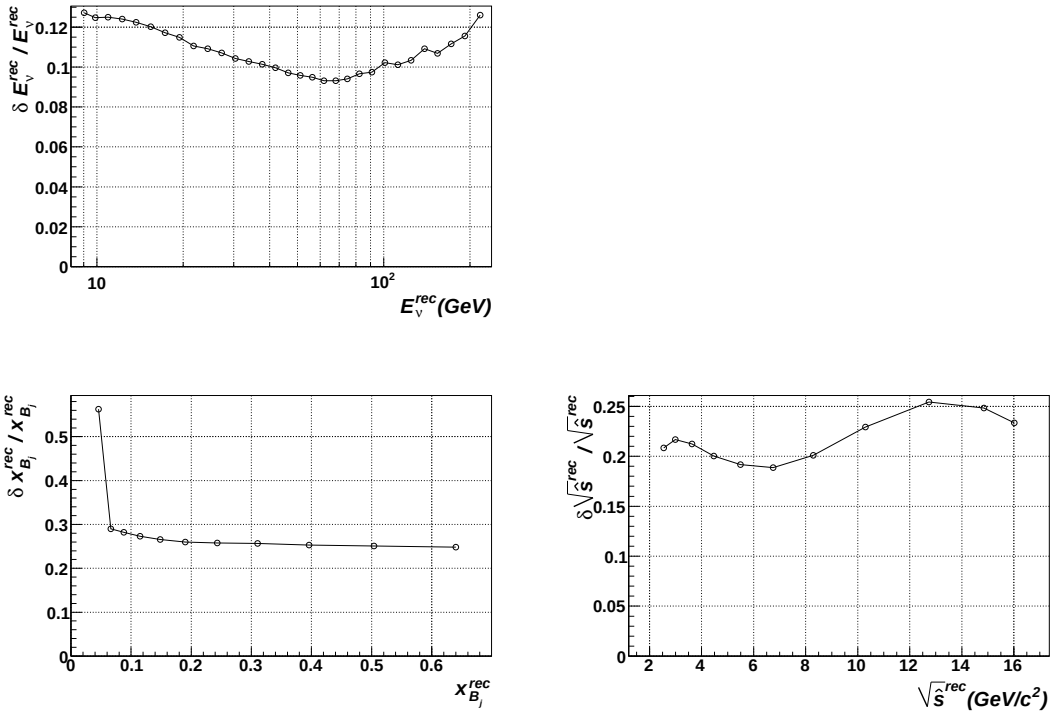

Fig. 21. *Relative resolution of the main kinematic variables: E_ν (top right), x_{B_j} (bottom left), $\sqrt{\hat{s}}$ (bottom right).*

We apply a similar re-weighting procedure to the inclusive ν_μ CC events (single muons). The model used for the inclusive CC structure functions on iron is the same described above for the charm production. The light quark contributions to the SFs are calculated in the NNLO QCD approximation. Figure 20 shows a comparison between data and weighted MC for different kinematic variables in ν_μ CC events.

4.2 Binning and hadronic energy correction

The binning of the data is performed in such a way that the size of each bin is comparable to the experimental resolution within that given bin. This procedure allows a reduction of correlations among different bins, thus minimizing systematic uncertainties. Figure 21 shows the relative resolution of the kinematic variables used for the $\mathcal{R}_{\mu\mu}$ measurement. Overall we have 19 bins for E_ν, 14 bins for x_{Bj} and 15 bins for $\sqrt{\hat{s}}$.

After defining the binning we perform a calibration of the global hadronic energy scale. This procedure corrects for potential discrepancies between data and MC related to the simulation of neutral and charged particles in the hadronic jet orginated by the neutrino-nucleus interactions. We perform the calibration of the hadronic energy scale by using the $y_{Bj} = E_{\rm Had}/E_\nu$ distribution in inclusive ν_μ CC events (single muon events). For each of the 19 bins in the *reconstructed* visible energy E_ν, we multiply the hadronic energy $E_{\rm Had}$ in MC events by a free scale factor k_{rmH}, and we detemine the optimal value of $k_{\rm H}$ by minimizing the χ^2 calculated from the $y_{\rm Bj}$ distribution in data and MC. This technique relies upon the precise measurement of E_μ in the drift chambers. Figure 22 summarizes the results of the χ^2 minimization. The best fit values for $k_{\rm H}-1$ range from -0.1% to -3.7%, depending upon the bin considered. Finally we interpolate the corrections for each bin with a spline function in order to have a smooth behavior of the hadronic energy scale as a function of the visible energy which can be extrapolated to different binning definitions. Our final results for the correction factor $k_{\rm H}$ are shown in Table 6 for all 19 E_ν bins. The use of a separate calibration factor $k_{\rm H}$ for each E_ν bin effectively takes into account differences in the development of the hadronic shower as a function of the neutrino energy (e.g. missing particles, fragmentation etc.). In general, we observe that the hadronic energy correction increases with the neutrino energy. As can be seen from Figure 23 the calibration of the global hadronic energy improves the agreement between data and MC for the y_{Bj} distribution.

In order to estimate the corresponding uncertainties on $k_{\rm H}$ we inflate the MC errors until the values of χ^2/dof at the minimum is equal to unity for each bin. We then calculate the 1σ error band as the range in $k_{\rm H}$ which is resulting in

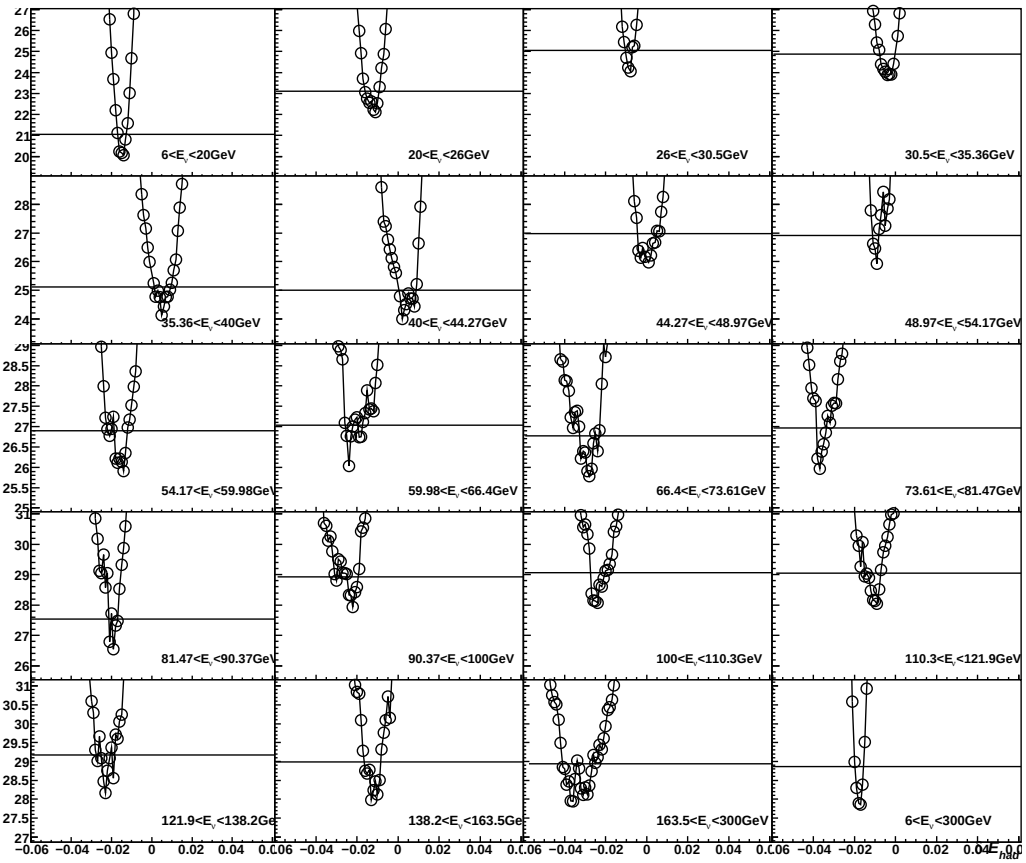

Fig. 22. *Calibration of the global hadronic energy scale. The curves show the values of χ^2 between data and rescaled MC obtained from the y_{Bj} distribution as a function of the scale correction ($k_{\rm H}-1$). The uncertainties in the MC have been inflated so that the χ^2/dof at the minimum is equal to unity for all bins.*

$\Delta\chi^2 = 1.0$. The uncertainties obtained for all bins are shown in Table 6 and go from 0.3% at low energy to about 1% at high energy.

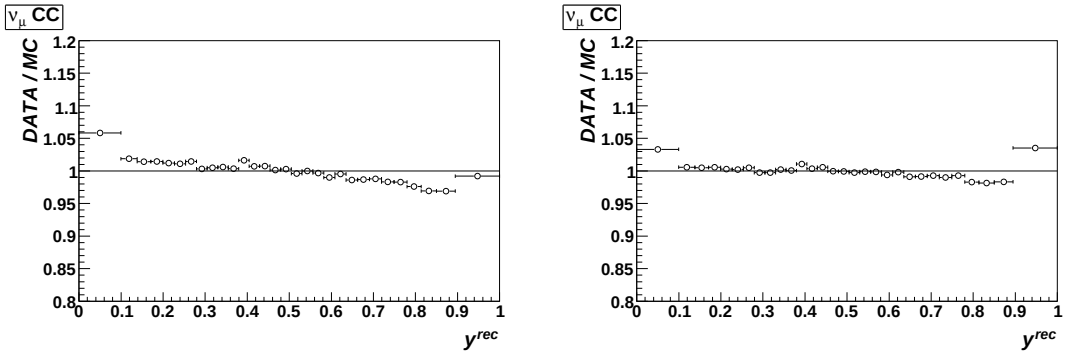

Fig. 23. *Ratio of data and MC for the y_{Bj} distribution before (left plot) and after (right plot) the calibration of the global hadronic energy scale.*

E_ν range	$k_{\rm H}$	1σ band
6 - 20	0.985	-0.003 +0.002
20 - 26	0.989	-0.006 +0.002
26 - 30.5	0.994	-0.003 +0.001
30.5 - 35.36	0.997	-0.004 +0.005
35.36 - 40	0.999	-0.004 +0.005
40 - 44.27	0.999	-0.003 +0.007
44.27 - 48.97	0.997	-0.006 +0.005
48.97 - 54.17	0.992	-0.003 +0.001
54.17 - 59.98	0.985	-0.008 +0.002
59.98 - 66.4	0.978	-0.002 +0.007
66.4 - 73.61	0.972	-0.008 +0.003
73.61 - 81.47	0.968	-0.002 +0.005
81.47 - 90.37	0.968	-0.001 +0.003
90.37 - 100	0.970	-0.009 +0.003
100 - 110.3	0.974	-0.004 +0.004
110.3 - 121.9	0.976	-0.008 +0.002
121.9 - 138.2	0.977	-0.005 +0.003
138.2 - 163.5	0.973	-0.004 +0.005
163.5 - 300	0.963	-0.006 +0.011
6 - 300	0.983	-0.003 +0.002

Table 6
Summary of the results for the calibration of the overall hadronic energy. For each bin in the *reconstructed* visible energy E_ν the final correction $K_{\rm H}$ and the 1σ band are listed.

4.3 Smearing matrix and efficiency correction

After re-weighting the MC events to our cross-section model, we unfold the detector response from the measured data for both the inclusive ν_μ CC and the charm dimuon events. To this end we first determine the smearing matrix and the efficiency corrections from the MC simulation:

$$N_i^{rec}(x^{rec}) = \sum_j r_{ij}(x^{rec}, x^{sim}) \times \epsilon_j(x^{sim}) \times N_j^{sim}(x^{sim}) \qquad (18)$$

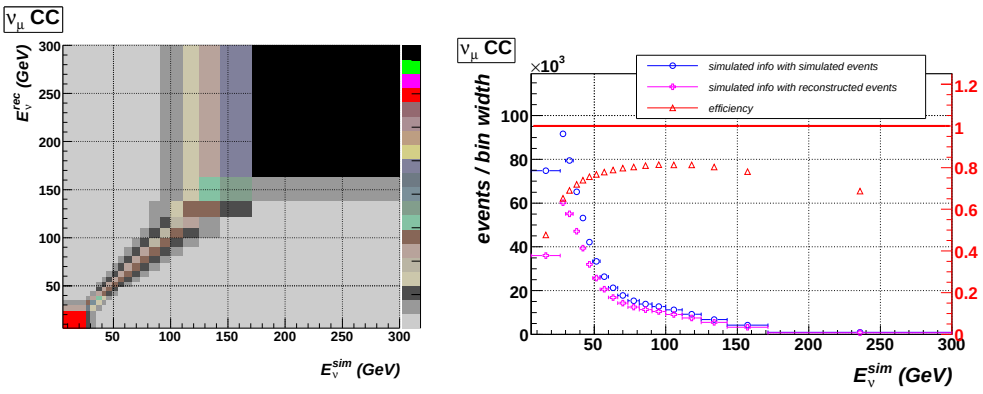

Fig. 24. *Example of resolution matrix* $r_{ij}(E_\nu^{rec}, E_\nu^{sim})$ *(left) and efficiency correction* $\varepsilon_j(E_\nu^{sim})$ *used in the unfolding of the neutrino energy distribution for* ν_μ *CC events.*

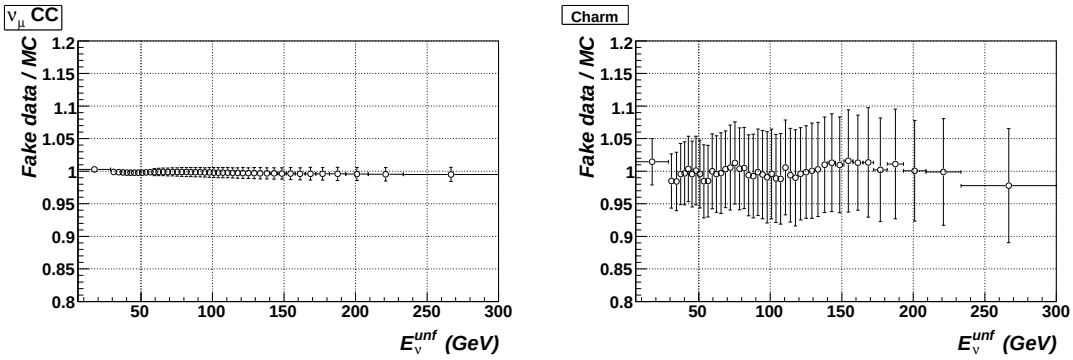

Fig. 25. *Check of the unfolding procedure for* $\nu_\mu CC$ *(left) and charm dimuon events (right). The plots show the ratio between the final unfolded variable and the input simulated variable for the unbiased MC sample not used to extract the resolution matrix and the efficiency (see text for details).*

where x^{rec} and x^{sim} are the reconstructed and simulated variable x ($x = E_\nu, x_{Bj}, \sqrt{\hat{s}}$). The inverse of the above relation provides the unfolded measurement:

$$N_j^{sim}(x^{sim}) = \sum_i \epsilon_i^{-1}(x^{sim}) \times r_{ji}^{-1}(x^{sim}, x^{rec}) \times N_i^{rec}(x^{rec}) \qquad (19)$$

Figure 24 shows an example of the resolution matrix and of the efficiency correction used in the analysis. The impact of non-diagonal terms in the smearing matrix is reduced because the bin size is comparable to the experimental resolution.

We validate the unfolding procedure by splitting the available MC events in two independent samples. The first sample (biased) is used to extract the smearing matrix and the efficiency correction. The second half of the MC sample (unbiased) is used as fake data to determine the unfolded distributions. These latter are then compared with the input simulated variables of

the unbiased sample. The results shown in Figure 25 demonstrate we can reproduce the input distributions in the unbiased sample with a good accuracy for both ν_μ CC and charm dimuon events. Finally we compare the unfolded distributions obtained from FCAL data and MC with an analytical calculation performed by convoluting our cross-section model with the neutrino flux. The results are shown in Figures 27 and 26.

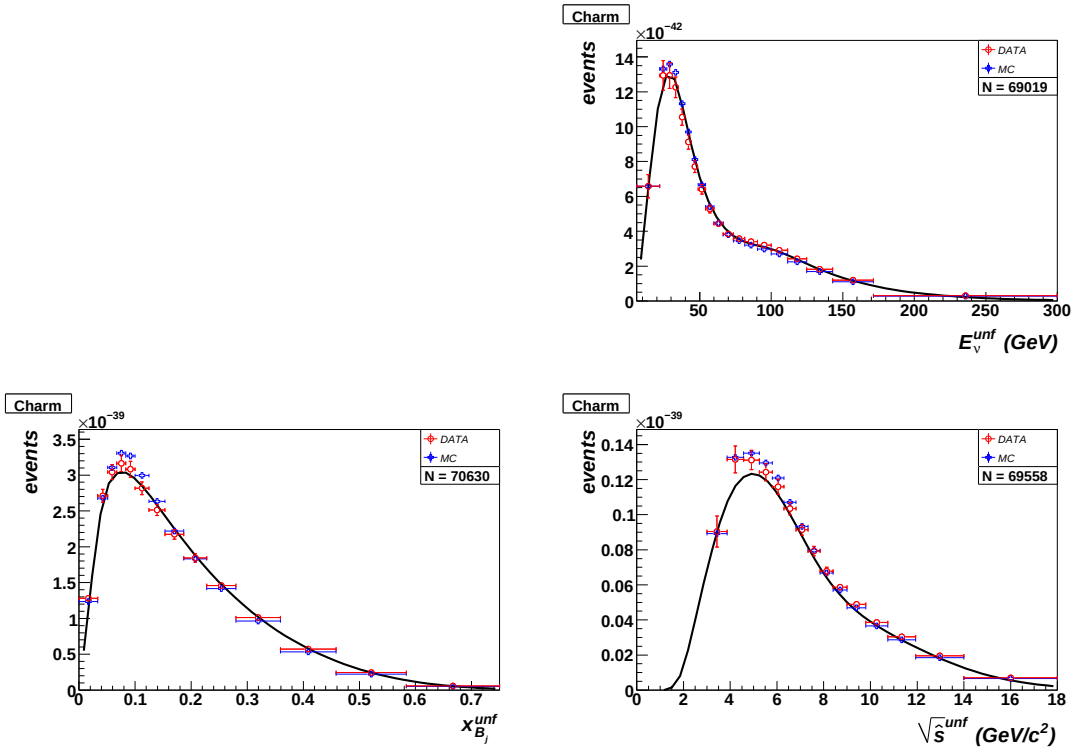

Fig. 26. *Comparison of unfolded data (open circles), unfolded MC (open crosses) and the corresponding analytical calculation taking into account $\sigma \times \Phi$ for the main kinematic variables in charm dimuon events: E_ν (top right), x_{B_j} (bottom left) and $\sqrt{\hat{s}}$ (bottom right).*

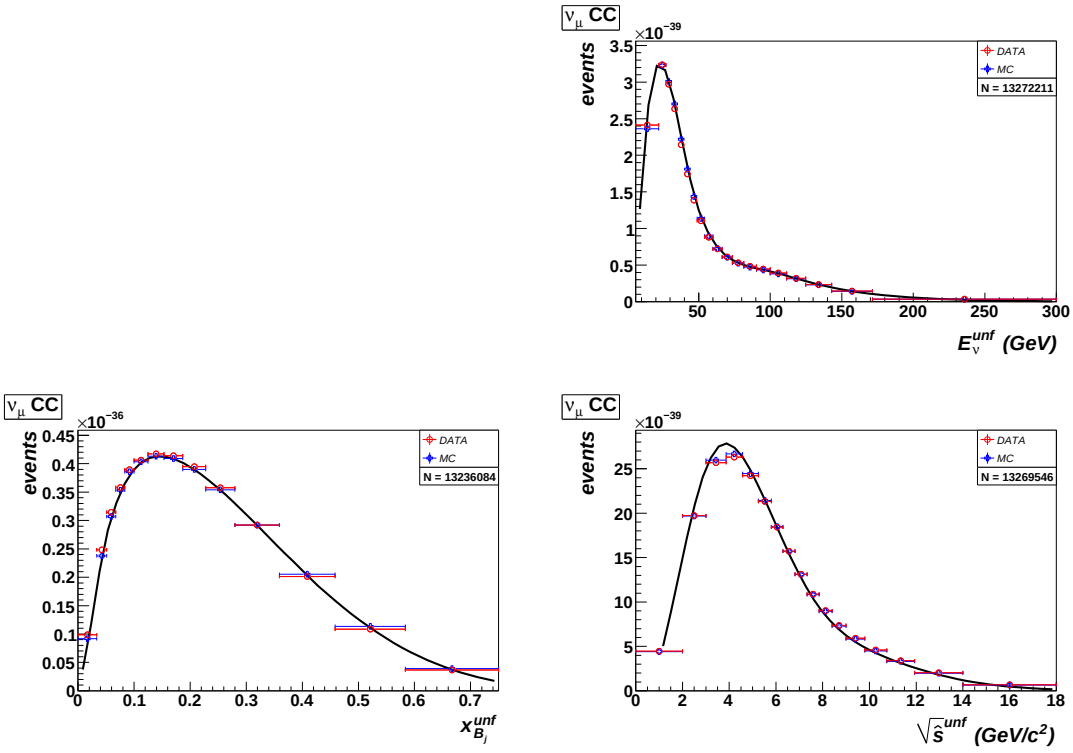

Fig. 27. *Comparison of unfolded data (open circles), unfolded MC (open crosses) and the corresponding analytical calculation taking into account $\sigma \times \Phi$ for the main kinematic variables in ν_μ CC events: E_ν (top right), x_{B_j} (bottom left) and $\sqrt{\hat{s}}$ (bottom right).*

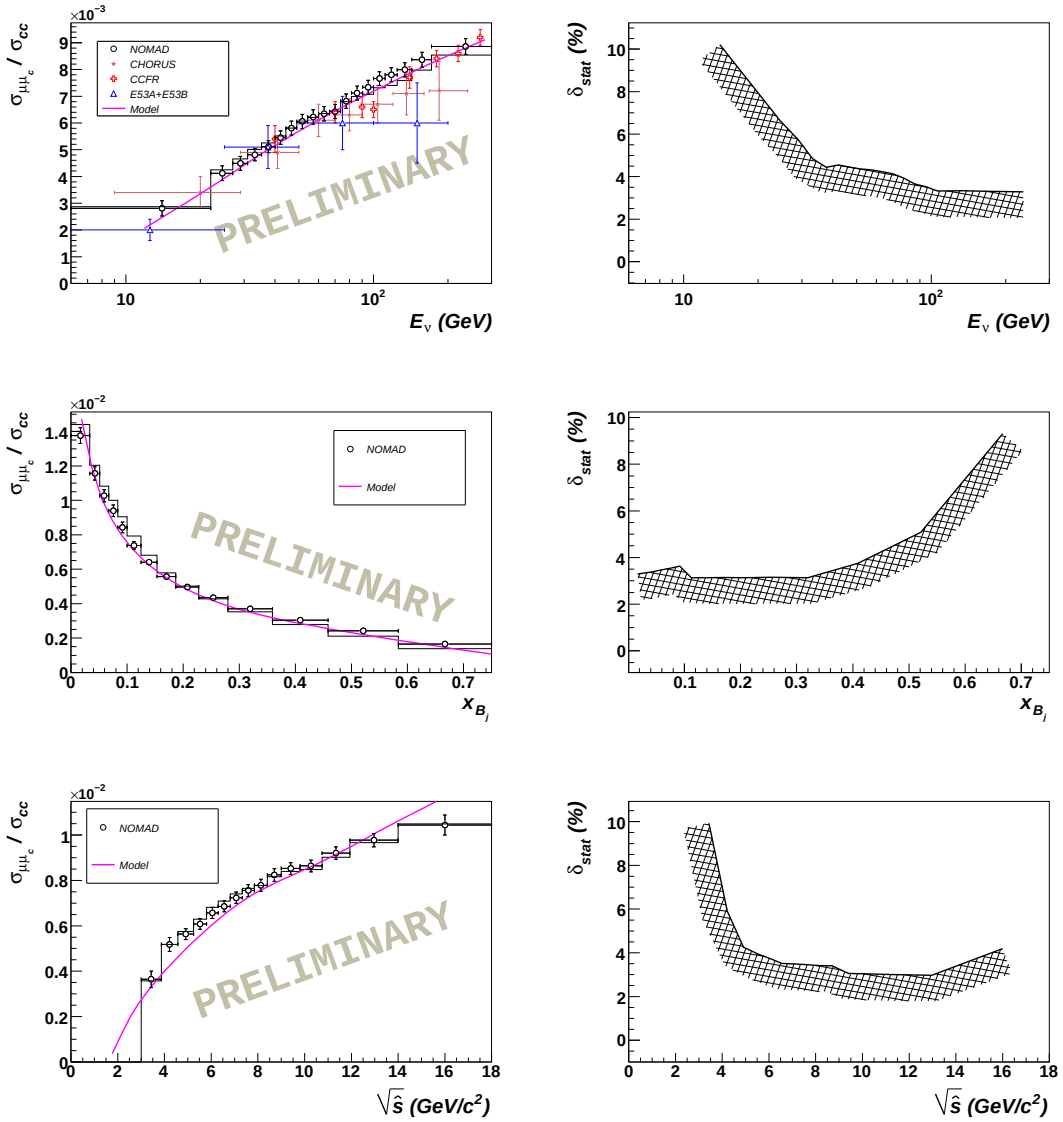

Fig. 28. *Ratio $\mathcal{R}_{\mu\mu}$ between charm dimuon cross-section and inclusive ν_μ CC cross–section as a function of kinematic variables: visible neutrino energy (top), x-Bjorken (middle) and center of mass energy $\sqrt{\hat{s}}$ (bottom). Only statistical uncertainties are shown and no bin centering correction is applied. The curves on the right plots give the relative statistical uncertainty in percentage. The solid curves represent the result of an analytical calculation fully independent from NOMAD data and based upon our cross-section model (see text for details). A comparison with previous measurements is also given in the top plot for completeness.*

5 Results

5.1 Charm fragmentation

The measured kinematic distributions for charm events are sensitive to the charm fragmentation function, which is giving the probability for the charmed hadron to carry a given fraction z of the longitudinal momentum of the hadronic system. We model the charm fragmentation function with the Collins-Spiller parameterization [16] shown in Equation (5), which has a more accurate asymptotic behavior in the limit of $z \to 1$ than the Peterson form [17]. The charm fragmentation function is folded with the NLO charm cross-section [1] through the re-weighting procedure implemented for all our MC events. This procedure allows a variation of the free parameter ε in the Collins-Spiller fragmentation function, together with the charm production parameters in the charm cross-section. We use two kinematic distributions to detemine ε from NOMAD data: the energy of the secondary muon from charm decay, E_{μ_c}, and the scaling variable x_{Bj}. The first one gives the most sensitive variable to fragmentation and has the advantage that it is largely independent from the details of the development of the hadronic shower inside FCAL, since the muon momentum is precisely measured in the drift chambers. Some additional sensitivity can be obtained from x_{Bj}, while the remaining kinematic variables do not add any substantial contribution. We perform a simultaneous fit to both E_{μ_c} and x_{Bj} by varying ε on an event-by-event basis in our MC re-weighting. The results are shown in Figure 29 and Table 7. The correlation with the mass of the charm quark m_c and with the strange sea parameterization turns out to be small in our fit since we mostly rely on the energy of the secondary muon E_{μ_c} to extract ε. A two-dimensional fit to E_{μ_c} and x_{Bj} with both ε and m_c as free parameters results indeed in a χ^2 surface which is flat as a function of m_c.

Experiment	NOMAD (E_{μ_c}, x_{Bj})	E531 (z_{C})	NOMAD + E531
ε	$0.165^{+0.035}_{-0.029}$	0.169 ± 0.036	0.165 ± 0.025

Table 7
Best fit values for the Collins-Spiller fragmentation parameter by using different data sets. See text for details.

In order to reduce the uncertainty in the determination of ε, we also consider the direct measurement of charm production performed by the E531 [18] experiment in nuclear emulsions. We re-fit the z_{C} distribution of the charmed mesons published by E531 with the Collins-Spiller function. The value of ε we obtain from E531 data is shown in Table 7 and is in good agreement with the value from the NOMAD analysis. We then use both the NOMAD and E531

data in a combined fit and obtain:

$$\varepsilon = 0.165 \pm 0.025$$

which is our final result. We use this value in the following analysis. Figure 29 shows the χ^2 curve from the combined fit.

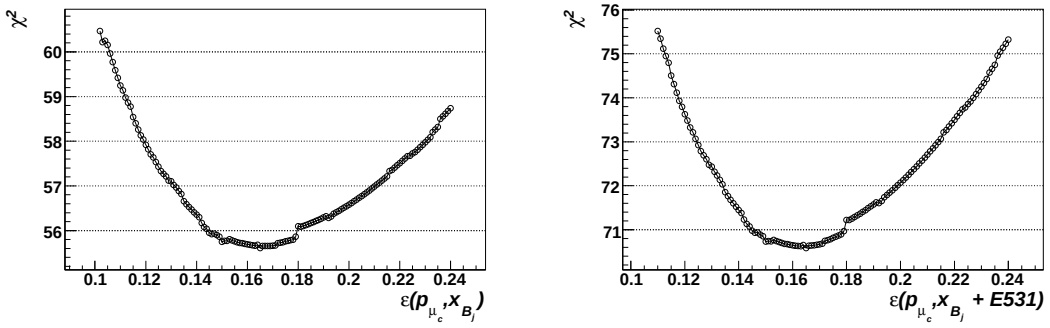

Fig. 29. *Determination of the ε parameter in the Collins-Spiller fragmentation function for charm hadrons from different data sets: fit to the E_{μ_c} and x_{B_j} distributions from NOMAD charm dimuon data (left), combined fit to both NOMAD and E531 data (right). The uncertainties have been scaled in order to obtain a value of χ^2/dof at the minimum equal to unity.*

Experiment	a	b (GeV)
E531	0.094 ± 0.010	6.6 ± 3.9
E531+NuTeV+CCFR	0.086 ± 0.006	4.1 ± 2.5
E531+NOMAD	0.094 ± 0.004	6.0 ± 1.6
E531+NOMAD+NuTeV+CCFR	0.094 ± 0.003	5.6 ± 1.4

Table 8
Coefficients of the energy dependent function used to parameterize B_μ obtained from different data sets.

5.2 Semileptonic branching ratio B_μ

The effective semileptonic branching ratio B_μ depends upon the energy of the incoming neutrino. The main reason is that the charmed fractions f_h for neutrino interactions are a function of the neutrino energy. This fact can be explained by the contributions from quasi-elastic Λ_c^+ and diffractive D_s^+ production. We note Λ_c^+ and D_s^+ have lower branching ratios into muon and therefore we expect the effective B_μ to decrease with neutrino energy. These two contributions are significant mainly at low energies and they would not affect much the value of B_μ at $E_\nu > 40$ GeV. Since NOMAD dimuon data extend down to $E\nu \sim 6$ GeV we need to take into account the energy dependence of B_μ in our analysis.

The only existing measurement of the charmed fractions f_h as a function of the neutrino energy comes from a re-analysis [19] of the data from the E531 experiment [8,18]. A new determination of B_μ as a function of the neutrino energy was obtained in Ref. [1] from the E531 emulsion data. We fit the data from Ref. [1] with the following smooth function:

$$B_\mu(E_\nu) = \frac{a}{1 + b/E_\nu} \tag{20}$$

which has two free parameters a and b. The values of the parameters obtained from a fit to E531 data are given in Table 8. Figure 30 shows the results of the fit together with the 1σ uncertainty band on B_μ obtained from a global fit to the NuTeV and CCFR charm dimuon data for $E_\nu > 30$ GeV [1]. The E531 data are consistent with the constant value of B_μ extracted at high energy from NuTeV and CCFR data in the common energy range. In the following we use the function in Equation (20) to parameterize B_μ in our analysis. If we add the NuTeV and CCFR dimuon data to the E531 data and extract the a and b parameters from the corresponding global fit we reduce the uncertainties on a and b by almost a factor of two, as can be seen from Table 8.

5.3 Bin centering correction

Figure 28 shows the measured ratios $\mathcal{R}_{\mu\mu}$ as a function of the kinematic variables E_ν, x_{Bj} and $\sqrt{\hat{s}}$ after the complete unfolding procedure. The definition of the bin size is based on the procedure described in Section 4.2 for the *reconstructed* variables. The boundaries of the corresponding bins in the *simulated* variables are then slightly adjusted in order to keep the same statistical uncertainty as in the reconstructed variables.

The curves represent our model calculation based upon the global PDF fit including only NuTeV and CCFR data [1]. Our new NOMAD measurement is in agreement with the independent predictions obtained without any input from NOMAD data.

We evaluate the overall average dimuon production rate in NOMAD by integrating the measured cross-sections after the unfolding and obtain:

$$\int \sigma_{\mu\mu_c} \phi \; dx \; dy \; dE_\nu \quad = \quad 5.15 \pm 0.05 \times 10^{-3} \; \nu_\mu \mathrm{CC}$$

After verifying the consistency of the normalization of each kinematic distribution, we use this average value to constrain the normalization of the cross-section ratios $\mathcal{R}_{\mu\mu}$.

Since the $\mathcal{R}_{\mu\mu}$ functions vary inside the chosen bins, we need to apply a bin centering correction to the data shown in Figure 28. To this purpose we use

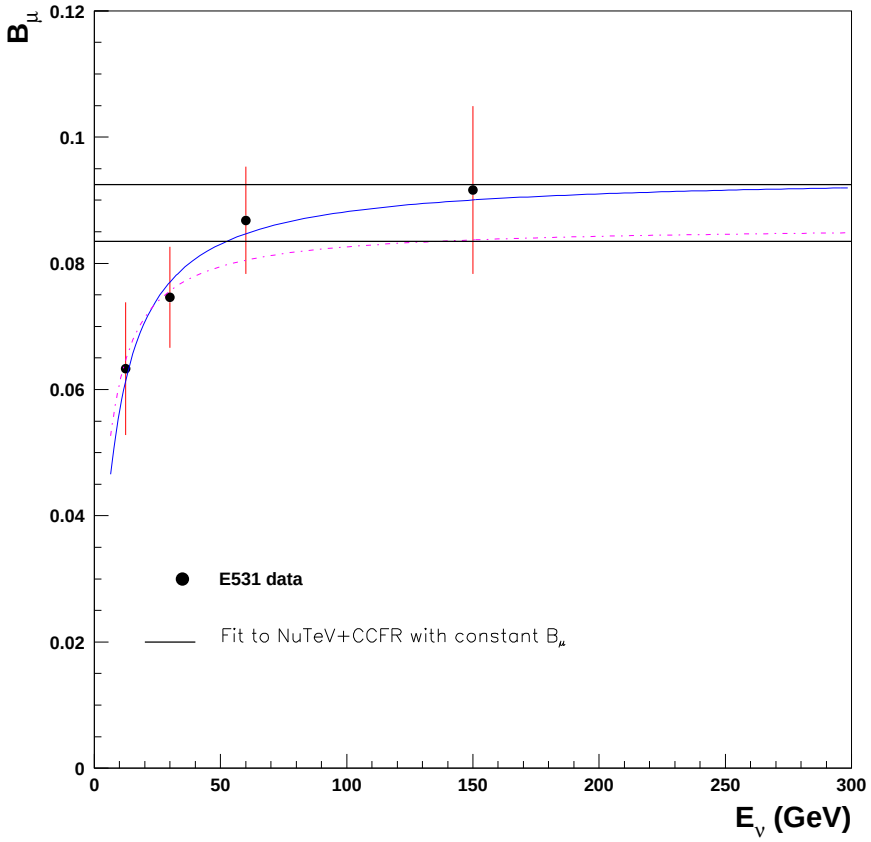

Fig. 30. *Extraction of the semileptonic branching ratio $B_\mu(E_\nu)$ from a fit to the E531 emulsion data (red points). The horizontal lines show the $\pm 1\sigma$ band obtained from a fit to NuTev and CCFR charm dimuon data assuming a constant value of B_μ independent of energy. The solid curve represents a fit to E531 data, while the dashed-dotted line is the result of a global fit to E531, NuTeV and CCFR data with the function in Equation (20).*

our model calculation convoluted with the NOMAD flux. For each bin, we find the value of the kinematic variable on the horizontal axis (E_ν, x_{Bj} or $\sqrt{\hat{s}}$) for which the analytical function $\mathcal{R}_{\mu\mu}$ is equal to the corresponding average value inside the bin. We then assign the measured value of $\mathcal{R}_{\mu\mu}$ for the bin considered to this calculated point on the horizontal axis. The final results are shown in Figure 31, Figure 32 and Figure 33.

6 Systematic uncertainties

The use of the *ratio* $\mathcal{R}_{\mu\mu}$ allows a substantial reduction of systematic uncertainties since all the effects related to both the numerator (charm dimuons)

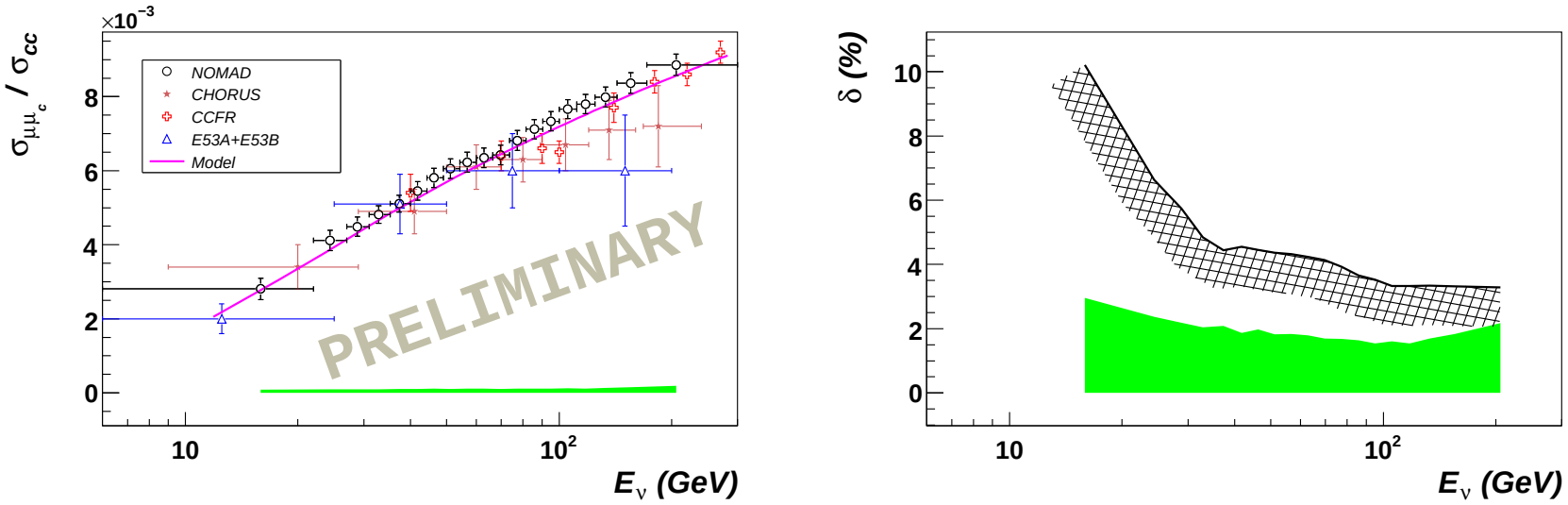

Fig. 31. *Final ratio $\mathcal{R}_{\mu\mu}$ between charm dimuon cross-section and inclusive ν_μ CC cross-section as a function of the neutrino energy. Both statistical and systematic uncertainties are shown and a bin centering correction was applied. The right plots give the relative statistical (black curve) and systematic (green band) uncertainties in percentage. The solid curves represent the result of an analytical calculation fully independent from NOMAD data and based upon our cross-section model (see text for details). A comparison with previous measurements is also given in the left plot for completeness.*

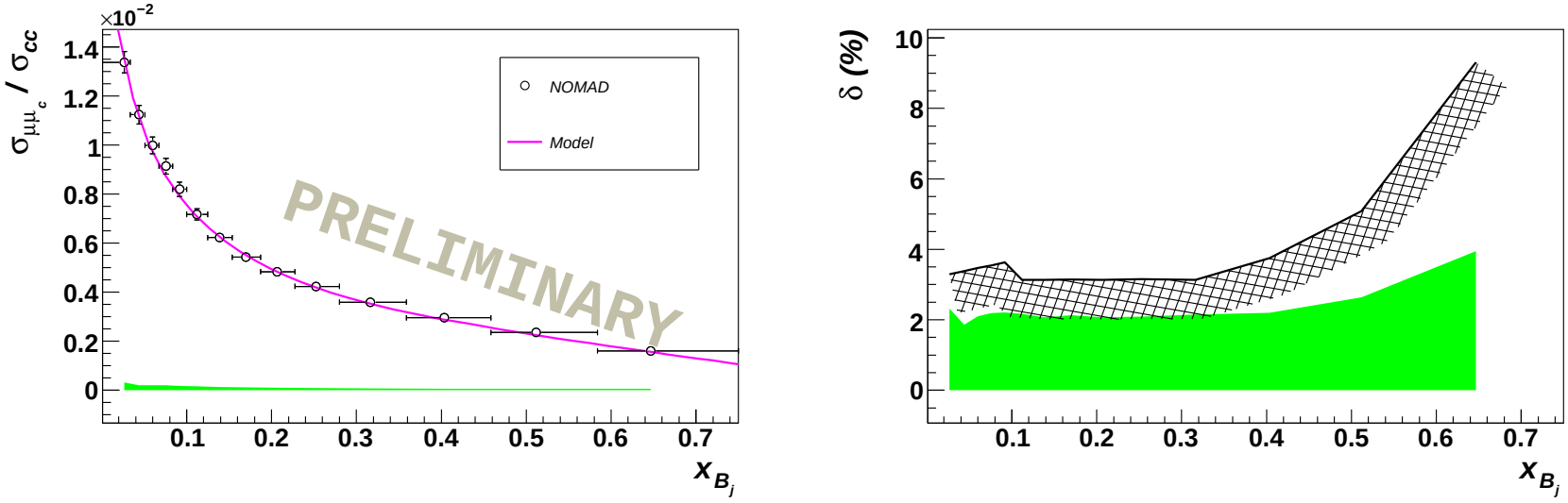

Fig. 32. *Final ratio $\mathcal{R}_{\mu\mu}$ between charm dimuon cross-section and inclusive ν_μ CC cross-section as a function of x-Bjorken. Both statistical and systematic uncertainties are shown and a bin centering correction was applied. The right plots give the relative statistical (black curve) and systematic (green band) uncertainties in percentage. The solid curves represent the result of an analytical calculation fully independent from NOMAD data and based upon our cross-section model (see text for details).*

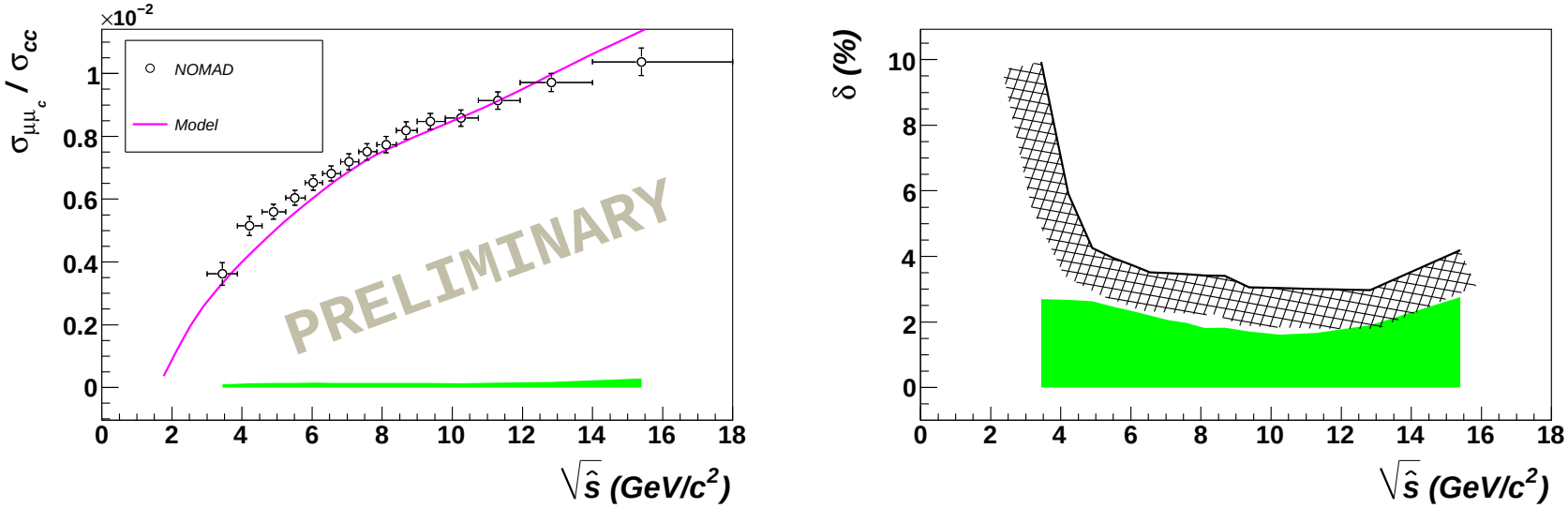

Fig. 33. *Final ratio $\mathcal{R}_{\mu\mu}$ between charm dimuon cross-section and inclusive ν_μ CC cross-section as a function of the center of mass energy $\sqrt{\hat{s}}$. Both statistical and systematic uncertainties are shown and a bin centering correction was applied. The right plots give the relative statistical (black curve) and systematic (green band) uncertainties in percentage. The solid curves represent the result of an analytical calculation fully independent from NOMAD data and based upon our cross-section model (see text for details).*

and the denominator (inclusive ν_μ CC) largely cancel out in the ratio. This cancellation applies to the experimental systematics as well as to the model systematics. To this end, the selection procedure is chosen to be as similar as possible between the 2μ and 1μ samples. Furthermore, we only rely on loose analysis cuts in order to minimize potential biases on the samples.

Figure 31, Figure 32 and Figure 33 show the final total systematic uncertainties, which are smaller than the statistical ones for all bins and kinematic variables. In most cases the oveall systematic uncertainty can be kept around 2%, as summarized in Table 9, Table 11 and Table 13. The total systematic uncertainty is dominated by the contributions directly related to the determination of the charm dimuon signal and therefore affecting only the numerator of the ratio $\mathcal{R}_{\mu\mu}$: background scale, charm fragmentation and mass of the charm quark m_c. The first one is entering directly in the background subtraction procedure, while the last two only enter through the acceptance correction.

A detailed breakdown of the contributions from each source of systematic uncertainty is given in Table 10, Table 12 and Table 14. The sign in front of the numbers refers to a variation of $+1\sigma$ of the corresponding effect and shows the bin-to-bin correlation. The magnitude of each systematic uncertainty is estimated as the average between positive ($+1\sigma$) and negative (-1σ) variations of the relevant parameters. We also change the number of bins in each kinematic variable from the nominal value to 25 and 45 (3 complete estimates) in order to check potential biases related to the bin size.

In the following we will describe the procedure we used to estimate the systematic uncertainties.

6.1 Variation of the analysis cuts

As discussed in Section 3.3, there is a good agreement between data and MC for the variables used in the selection procedure and for the final kinematic distributions in both charm dimuon events and inclusive ν_μ CC events. Therefore, the systematic uncertainty associated to each analysis cut is essentially defined by the experimental resolution of the relevant variable for values close to the chosen cut. We evaluate the experimental resolutions from the difference between reconstructed and simulated variables in MC events close to the chosen cuts. We fit the corresponding distributions with gaussian functions and we vary each cut by the resulting standard deviation from the fit.

The effect of a variation of the analysis cuts according to the experimental resolution is very small on the ratio $\mathcal{R}_{\mu\mu}$. The following effects have been taken into account:

δ_1 $|x_{ext}^{PV}| < 80$ cm.
From Figure 34 we take $\delta(x_{ext}^{PV}) \simeq 0.6$ cm (0.75%).

δ_2 $|y_{ext}^{PV}| < 90$ cm.
From Figure 34 we take $\delta(y_{ext}^{PV}) \simeq 0.7$ cm (0.75%).

δ_3 Time correlation between two muons less then 5 ns.
The timing of the muons is provided by the t_0 measurement at the first track hit in the drift chambers resulting in $\delta(t_0) \sim 1$ ns (20%).

δ_4 Energy of the current muon more then 3 GeV.
From Figure 35 we take $\delta(E_{\mu_{cc}}) = 162$ MeV (5.4%).

δ_5 Energy of the secondary muon from charm decay > 3 GeV ($E_{had} > 3$ GeV).
From Figure 35 we take $\delta(E_{\mu_c}) = 165$ MeV (5.5%).

δ_6 $Q^2 > 1$ GeV^2/c^2.
From Figure 36 we take $\delta(Q^2) = 0.30$ GeV^2 (30%).

δ_7 $E_{had} - E_{\mu^+} < 100$ GeV.
According to the FCAL energy resolution $\sigma(E)/E = 104\%/\sqrt{E}$ we take $\delta(E_{had} - E_{\mu^+}) = 10.4$ GeV at 100 GeV (10%).

6.2 Energy scales and flux

The impact of the energy scales and flux uncertainties on the rato $\mathcal{R}_{\mu\mu}$ is very small due to the large cancellation between charm dimuon events and ν_μ CC events.

δ_8 Muon energy scale.
The measurement of the muon momentum is performed by fitting the curvature of the track in the low density tracking region equipped with drift chambers (DC). The E_μ scale was determined by a precise B-field mapping and DC alignment accomplished by using several million beam muons traversing the detector throughout the neutrino runs. The momentum scale was checked by using the invariant mass of over 30000 reconstructed K_0 in the CC and NC data. The systematic uncertainty on the E_μ scale from DC was determined to be 0.2%.
The momentum of the muons at the first hit of the track in DC is extrapolated back to the position of the primary vertex in FCAL by adding the corresponding energy loss in the FCAL material. Figure 37 shows the calculated energy loss, $\Delta E_{\rm loss}$, in a single FCAL stack. Assuming a uniform distribution of the vertex position within each stack, we obtain a corresponding uncertainty of $\Delta E_{\rm loss}/\sqrt{12}$ due to the variable amount of material traversed by the muon. This contribution is dominant over the E_μ scale uncertainty from DC at low energy as can be seen from Figure 37. However, in our analysis we always assign to the event a *fixed z position* equal to the middle point of the stack in which the primary vertex is located. This fact implies that *on average* the energy loss in the FCAL material is

correctly taken into account. Therefore, the overall uncertainty on the E_μ energy scale is basically defined by the DC contribution. Figure 13 shows a good agreement between data and MC for the final extrapolated energy of the muons.

δ_9 Hadronic energy scale.
For the estimate of the systematic uncertainty on the global hadronic energy scale we start from the results obtained in Section 4.2. We repeat the calibration of the hadronic energy scale after restricting the fiducial volume to $\mid x, y \mid < 70$ cm and after changing the kinematic cuts used in the selection. We then compare the variations observed for the scale factor with the uncertainty band obtained in the original fit with $\Delta\chi^2 = 1$. Figure 38 summarizes the results as a function of the visible energy E_ν. We define our final uncertainty band by taking an outer envelope over the average of postive ($+1\sigma$) and negative (-1σ) variations. This band is consistent with the variations observed after changing the analysis cuts, as shown in Figure 38. The size of the $E_{\rm had}$ scale uncertainty goes from 0.3% in the first energy bin to about 1% in the last energy bin.

δ_{10} Beam flux prediction.
In our analysis we use a beam flux calculation based upon Ref. [20]. The spectra for FCAL are slightly harder due to the restricted transverse size of the FCAL fiducial volume. We obtain the FCAL flux by applying the same fiducial cuts used in our analysis to the Nubeam ntuples re-weighted by the SPY parameterizations. Figure 39 shows the final flux prediction for FCAL together with the corresponding uncertainty from Ref. [20].

6.3 Model systematic uncertainties

The modeling of the charm dimuon production and the background subtraction procedure in the dimuon sample are the dominant sources of systematic uncertainties. Other systematic effects related to the modeling of the structure functions affecting both the charm dimuon sample and the inclusive ν_μ CC sample give very small contributions. For each contribution, we repeat the complete analysis after changing the relevant paramenters by $\pm 1\sigma$. In the following we describe the variations of the parameters used.

δ_{11} Background scale.
As discussed in Section 3.3.1, our background subtraction procedure in entirely based upon NOMAD data. The uncertainty on the background scale, i.e. on the ratio $N_{\mu\mu^+_{bg}}/N_{\mu\mu^-}$, is constrained by the measurement of the ratio h^+/h^- of positive to negative hadrons in DCH. We use the uncertainty band from the fit to the measured ratio, including the full correlation matrix, as shown in Figure 40.

δ_{12} Charm fragmentation.

We vary the ε parameter in the Collins-Spiller fragmentation function within the uncertainty obtained from the fit to NOMAD+E531 data, $\pm\Delta\varepsilon = 0.025$ (see Section 5.1).

The acceptance correction is obtained from the MC simulation, which takes into account the decay of each charmed hadron according to the recent branching ratios [21]. The charmed fractions f_h are the ones provided by the E531 data [19]. We varied the charmed fractions f_h and the muon branching ratios of individual hadrons within their experimental uncertainties in our MC. The corresponding changes in the acceptance correction were found to be negligible.

δ_{13} Mass of charm quark m_c.

We vary the value of the mass of the charm quak by $\pm\Delta m_c = 60$ MeV, which is the uncertainty band obtained from the global PDF fit of Ref. [1] with the addition of NOMAD dimuon data.

δ_{14} Structure functions (Leading Twist).

We change *all* parton density functions obtained from a global fit to charged lepton DIS data, CHORUS (anti)neutrino DIS data, NuTeV and CCFR dimuon data and Drell-Yan data within their uncertainties [1,10]. The variations include strange sea quark distributions.

δ_{15} High twists.

We include twist-4 power corrections to the neutrino structure functions following the results of Ref. [10]. For F_2 and F_T the High Twist contributions are obtained from charged lepton scattering DIS data after rescaling for the quark charges (18/5). For xF_3 the twist-4 term is obtained from the (anti)neutrino differential cross-section measured by the CHORUS experiment. We use the uncertainties obtained from the global fits of Refs. [10,1] to estimate the systematic uncertainties related to High Twists.

δ_{16} Electroweak corrections.

Radiative corrections to neutrino DIS are calculated according to the code developed for the NOMAD analysis [14]. The measured rato $\mathcal{R}_{\mu\mu}$ is not corrected for electroweak radiative effects in order to avoid model dependent corrections to the data. Therefore, the electroweak corrections only affect the measurement in an indirect way, through the detector acceptance. We evaluate the corresponding systematic uncertainties by varying the electroweak corrections within the uncertainty range from Ref. [14].

δ_{17} Nuclear corrections.

We apply nuclear corrections using a detailed model [11–13] taking into account a number of different effects including the Fermi motion and binding, neutron excess, nuclear shadowing, nuclear pion excess and the off-shell correction to bound nucleon structure functions. We use the uncertainties on the corresponding parameters provided by the analysis of charged lepton data in Ref. [13]. The uncertainties include target mass corrections [15], which are included into the nuclear convolution.

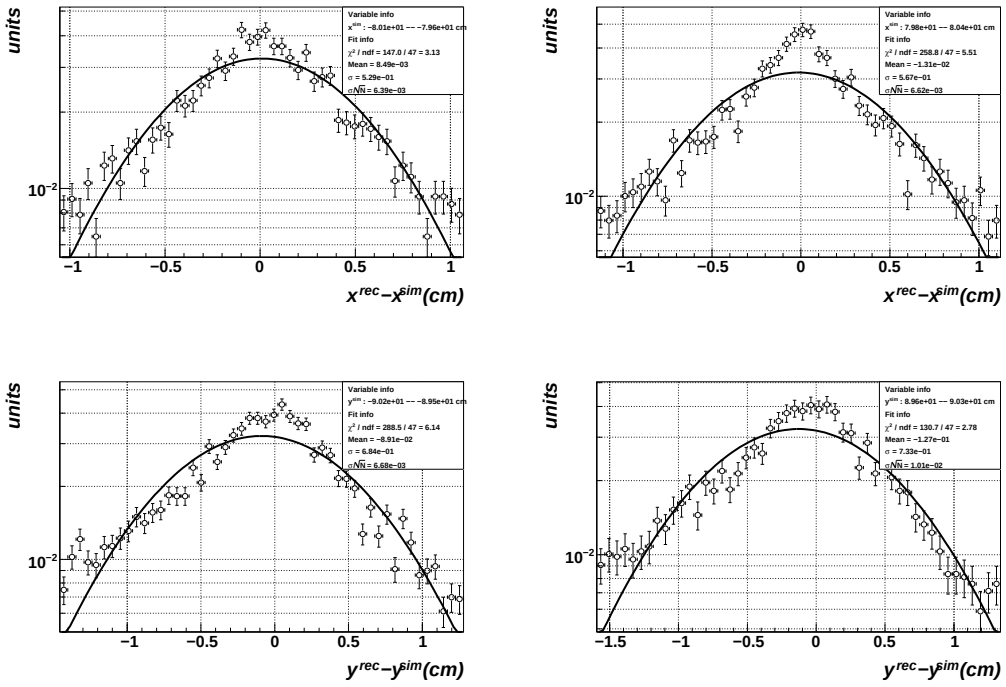

Fig. 34. *Resolution for FV cut:* $x_{ext}^{PV} > -80$ *cm (top left),* $x_{ext}^{PV} < 80$ *cm (top right),* $y_{ext}^{PV} > -90$ *cm (bottom left),* $y_{ext}^{PV} < 90$ *cm (bottom right).*

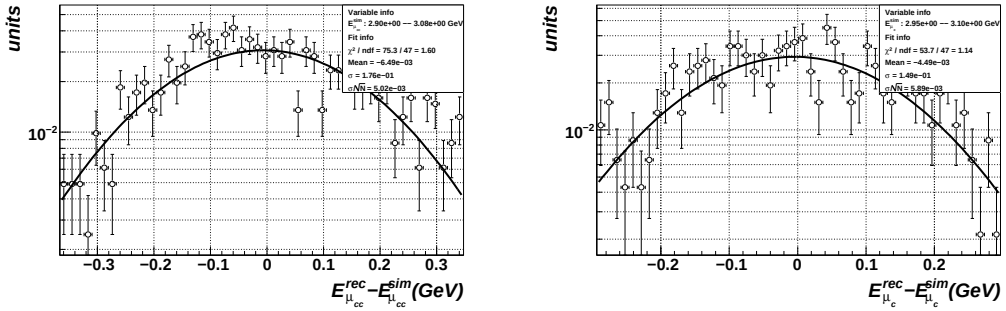

Fig. 35. *Resolution for muon energy:* $E_{\mu^-} \simeq 3$ *GeV (left),* $E_{\mu^+} \simeq 3$ *GeV (right).*

7 Determination of Charm Production Parameters

The unfolding correction factorizes out the detector acceptance from the measurement. Therefore, the resulting cross-sections can be directly compared with the analytical model to extract the charm production parameters, which include the mass of the charm quark, m_c, the effective semileptonic branching ratio, B_μ, and the strange sea parton distribution function, $s(x)$. We add NOMAD $\mathcal{R}_{\mu\mu}$ data to the global PDF fit described in Refs. [1] in order to satisfy QCD sum rules and the constraints on PDFs from charged lepton DIS

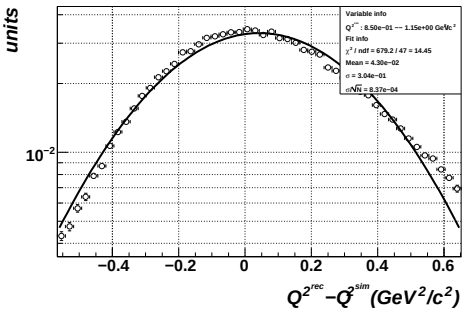

Fig. 36. *Resolution for* $Q^2 \simeq 1\ GeV^2$.

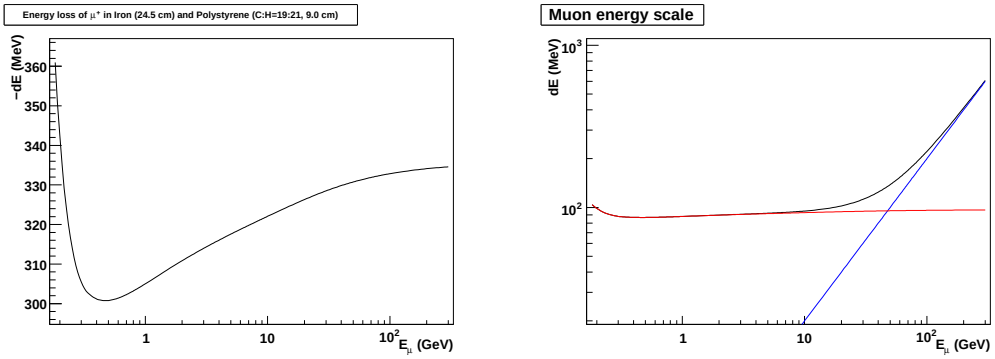

Fig. 37. *Energy loss by muons in a single FCAL stack (left plot). Contributions to the* E_μ *energy scale uncertainty (right plot).*

data and Drell-Yan data. Two variants of the global fit are performed. The first one (fit A) includes only the charm dimuon data from NOMAD, without the ones from NuTeV and CCFR. The second variant includes NuTeV and CCFR dimuon data as well (fit B). The fits are performed in the framework introduced by S. Alekhin in Ref. [22], which uses the running mass in the $\overline{\rm MS}$ scheme for DIS charm production. The calculation includes partial NNLO corrections for the coefficients of the charm heavy quark structure functions for DIS. The results for the $\overline{\rm MS}$ running mass, $m_c(m_c)$, the strange sea suppression factor, κ_s, and the parameters a and b entering the B_μ parameterization as a function of energy are summarized in Table 15 and Table 8.

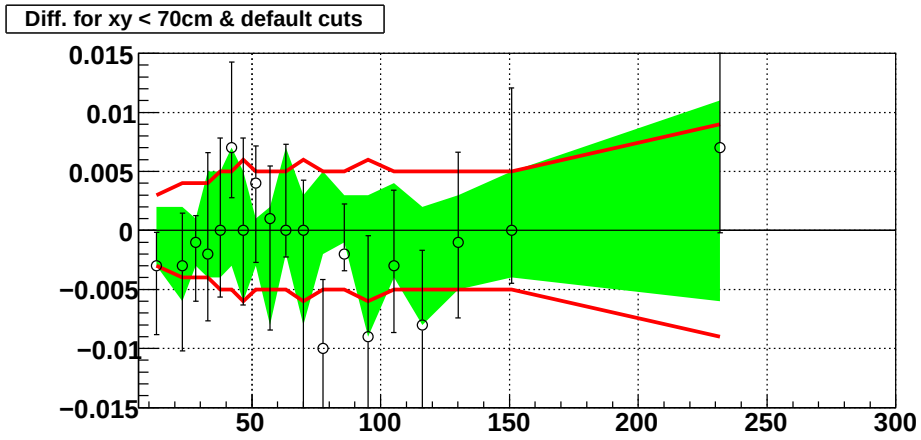

Fig. 38. *Systematic uncertainty of the global hadronic energy scale as a function of the neutrino energy. The green band is the uncertainty obtained with* $\Delta\chi^2 = 1$ *from the fit to the* y_{Bj} *distribution. The points show the difference obtained in the hadronic energy scale between the default cuts and a restricted fiducial volume* $\mid x, y \mid < 70$ *cm. The red curves show our final systematic uncertainty (see text for details).*

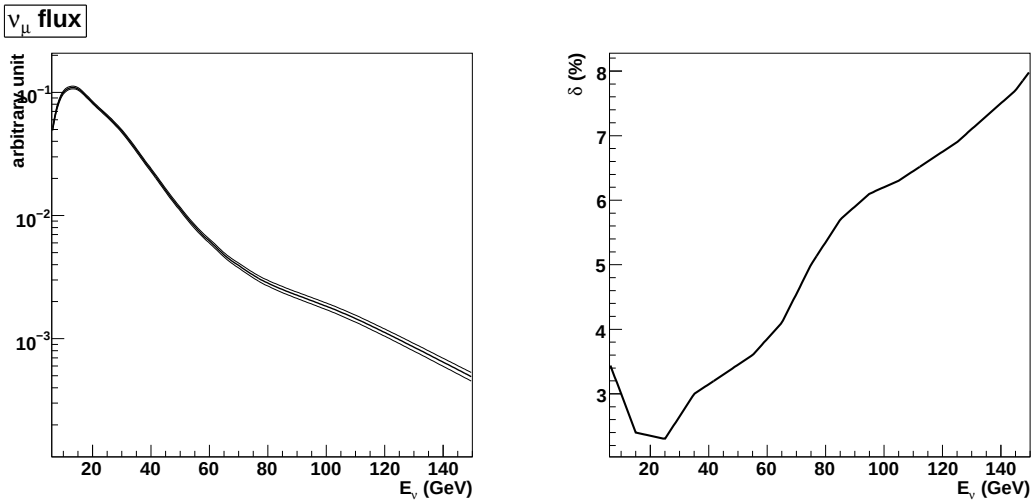

Fig. 39. *FCAL flux prediction (left) and its uncertainties (right) [20].*

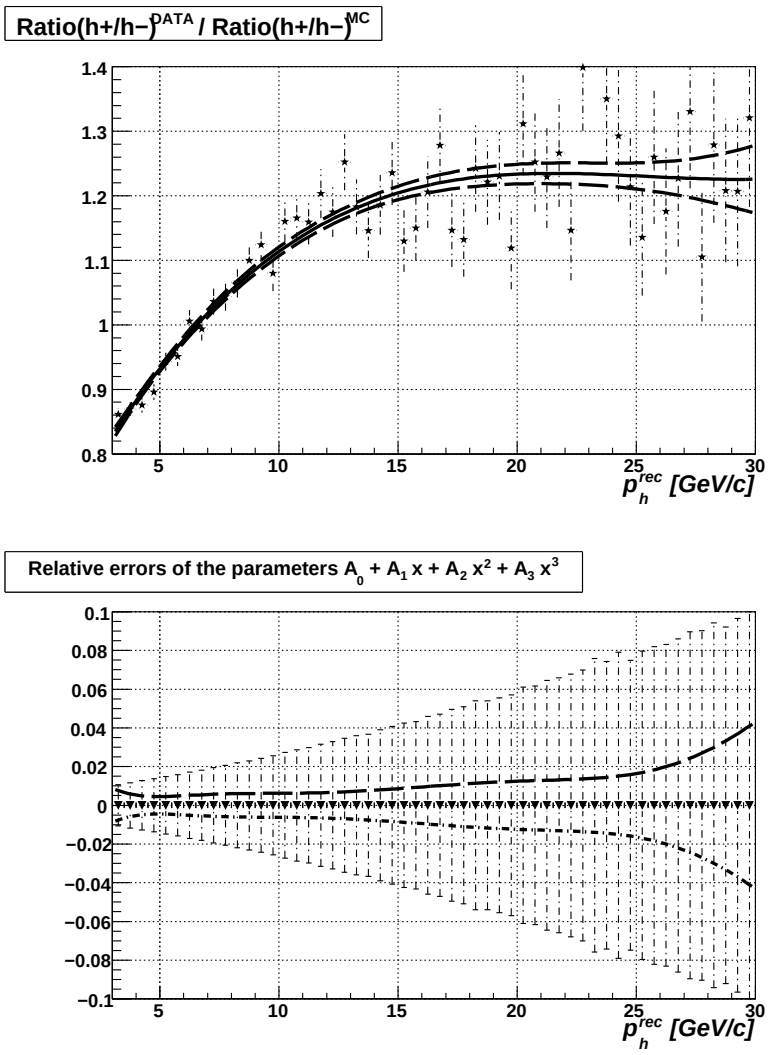

Fig. 40. *Uncertainty on the background scale factor. The top plot shows a fit to the measured ratio of positive to negative hadrons in DC. The bottom plot gives the* 1σ *uncertainty band (relative errors) compared with the statistical uncertainty of the measured points (dashed lines).*

E_ν	Bin center	$\sigma_{\mu\mu}/\sigma_{cc} \pm \delta^{stat} \pm \delta^{syst}$ (10^{-3})	δ^{stat}, %	δ^{syst}, %
6.000 - 22.00	15.91	2.807 ± 0.287 ± 0.083	10.22	2.96
22.00 - 27.00	24.38	4.118 ± 0.273 ± 0.098	6.63	2.37
27.00 - 31.00	28.85	4.489 ± 0.257 ± 0.098	5.73	2.19
31.00 - 35.34	32.88	4.815 ± 0.233 ± 0.098	4.85	2.04
35.34 - 40.00	37.31	5.113 ± 0.227 ± 0.107	4.44	2.08
40.00 - 44.27	41.78	5.453 ± 0.248 ± 0.102	4.55	1.87
44.27 - 48.97	46.23	5.807 ± 0.259 ± 0.115	4.46	1.98
48.97 - 54.17	51.17	6.056 ± 0.265 ± 0.111	4.37	1.83
54.17 - 59.98	56.73	6.227 ± 0.269 ± 0.114	4.32	1.83
59.98 - 66.40	62.87	6.348 ± 0.269 ± 0.113	4.23	1.79
66.40 - 73.61	69.70	6.425 ± 0.266 ± 0.109	4.14	1.70
73.61 - 81.47	77.29	6.816 ± 0.268 ± 0.115	3.93	1.68
81.47 - 90.37	85.78	7.121 ± 0.260 ± 0.116	3.66	1.64
90.37 - 100.0	95.01	7.337 ± 0.259 ± 0.113	3.53	1.54
100.0 - 111.4	105.4	7.660 ± 0.255 ± 0.123	3.33	1.60
111.4 - 124.7	117.6	7.800 ± 0.260 ± 0.120	3.33	1.54
124.7 - 142.9	133.0	7.989 ± 0.267 ± 0.135	3.34	1.69
142.9 - 171.4	155.4	8.368 ± 0.278 ± 0.153	3.32	1.83
171.4 - 300.0	205.5	8.859 ± 0.292 ± 0.192	3.29	2.17

Table 9

Measured $\mathcal{R}_{\mu\mu}$ as a function of visible neutrino energy E_ν including both statistical and total systematic uncertainties. The last two columns provide the corresponding relative uncertainties.

Bin / δ^{syst}, %	δ_1	δ_2	δ_3	δ_4	δ_5	δ_6	δ_7	δ_8	δ_9	δ_{10}	δ_{11}	δ_{12}	δ_{13}	δ_{14}	δ_{15}	δ_{16}	δ_{17}
6.000 - 22.00	0.24	-0.44	0.66	0.14	-0.53	-1.42	0.00	0.45	0.18	-0.18	-1.01	1.48	-1.50	0.02	-0.04	-0.01	0.18
22.00 - 27.00	0.22	-0.21	0.18	0.13	-0.40	-0.58	0.00	0.26	0.28	-0.16	-0.96	1.84	-0.70	0.00	0.02	-0.01	0.11
27.00 - 31.00	0.20	-0.16	0.26	0.13	-0.23	-0.28	0.00	-0.13	0.29	-0.10	-0.89	1.81	-0.54	0.00	0.01	-0.01	0.09
31.00 - 35.34	-0.11	-0.06	0.24	0.13	-0.20	-0.08	0.01	-0.17	0.25	-0.08	-0.88	1.74	-0.37	0.00	0.02	-0.01	0.07
35.34 - 40.00	-0.07	-0.08	0.25	0.10	-0.25	0.05	0.01	-0.16	0.24	-0.09	-0.88	1.79	-0.33	0.00	0.02	-0.01	0.07
40.00 - 44.27	-0.09	-0.10	0.31	0.07	-0.26	-0.03	0.02	-0.09	0.38	-0.07	-0.90	1.49	-0.36	0.00	0.02	-0.01	0.05
44.27 - 48.97	-0.05	-0.03	-0.30	0.04	-0.27	-0.13	0.03	-0.06	0.56	-0.05	-0.93	1.57	-0.32	0.00	0.02	-0.01	0.06
48.97 - 54.17	-0.07	-0.06	-0.31	0.02	-0.26	-0.20	0.03	0.06	0.42	-0.07	-0.95	1.39	-0.30	0.00	0.01	-0.01	0.04
54.17 - 59.98	0.09	0.10	-0.25	0.01	-0.27	-0.18	0.03	0.05	0.23	-0.08	-0.99	1.44	-0.25	0.00	0.01	-0.00	0.04
59.98 - 66.40	0.02	0.13	-0.21	0.01	-0.30	-0.15	0.03	0.12	0.24	-0.07	-1.01	1.36	-0.23	0.01	0.01	-0.01	0.04
66.40 - 73.61	0.07	-0.15	-0.14	0.02	-0.29	0.11	0.04	0.10	0.34	-0.03	-1.05	1.21	-0.20	0.00	0.02	-0.01	0.04
73.61 - 81.47	0.08	-0.10	-0.09	0.02	-0.26	0.14	0.02	-0.04	0.28	-0.03	-1.08	1.20	-0.20	0.00	0.01	-0.01	0.05
81.47 - 90.37	0.23	-0.08	-0.15	0.01	-0.24	0.13	0.04	0.03	0.28	0.06	-1.10	1.10	-0.12	0.00	0.01	-0.00	0.05
90.37 - 100.0	0.15	-0.11	-0.16	0.01	-0.24	0.14	0.09	0.05	0.37	0.06	-1.13	0.89	-0.17	0.00	0.01	-0.01	0.03
100.0 - 111.4	-0.17	-0.08	-0.12	-0.00	-0.26	0.15	0.14	0.05	0.27	0.06	-1.17	0.97	-0.14	0.01	0.02	-0.00	0.04
111.4 - 124.7	-0.11	-0.07	-0.13	-0.01	-0.24	0.13	0.19	0.06	0.28	0.10	-1.20	0.81	-0.09	0.00	0.01	-0.00	0.04
124.7 - 142.9	-0.19	-0.12	-0.21	-0.00	-0.23	0.15	0.59	0.04	0.34	0.05	-1.23	0.84	-0.02	0.00	0.01	-0.00	0.02
142.9 - 171.4	-0.15	-0.20	-0.25	-0.00	-0.12	0.17	0.73	-0.05	0.67	-0.14	-1.24	0.80	0.01	0.00	0.01	0.00	0.02
171.4 - 300.0	-0.22	0.18	-0.21	-0.00	0.11	0.20	-0.40	0.10	1.13	-0.81	-1.27	0.88	0.16	0.00	0.03	0.01	0.03

Table 10
Charm production.

x_{Bj}	Bin center	$\sigma_{\mu\mu}/\sigma_{cc} \pm \delta^{stat} \pm \delta^{syst}$ (10^{-3})	δ^{stat}, %	δ^{syst}, %
0.00000 - 0.03361	0.02673	13.383 ± 0.441 ± 0.311	3.30	2.32
0.03361 - 0.05106	0.04401	11.245 ± 0.380 ± 0.210	3.38	1.86
0.05106 - 0.06721	0.05978	9.991 ± 0.347 ± 0.209	3.47	2.10
0.06721 - 0.08356	0.07562	9.141 ± 0.324 ± 0.200	3.55	2.19
0.08356 - 0.1000	0.09167	8.198 ± 0.297 ± 0.181	3.63	2.21
0.1000 - 0.1246	0.1122	7.176 ± 0.225 ± 0.156	3.13	2.17
0.1246 - 0.1535	0.1389	6.229 ± 0.195 ± 0.129	3.14	2.07
0.1535 - 0.1870	0.1699	5.427 ± 0.171 ± 0.116	3.15	2.13
0.1870 - 0.2277	0.2066	4.837 ± 0.151 ± 0.100	3.13	2.07
0.2277 - 0.2800	0.2524	4.235 ± 0.133 ± 0.089	3.15	2.09
0.2800 - 0.3590	0.3165	3.595 ± 0.113 ± 0.077	3.13	2.15
0.3590 - 0.4583	0.4036	2.955 ± 0.111 ± 0.065	3.75	2.19
0.4583 - 0.5838	0.5116	2.355 ± 0.120 ± 0.062	5.08	2.64
0.5838 - 0.7500	0.6465	1.607 ± 0.150 ± 0.063	9.31	3.95

Table 11

Measured $\mathcal{R}_{\mu\mu}$ as a function of x_{Bj} including both statistical and total systematic uncertainties. The last two columns provide the corresponding relative uncertainties.

x_{Bj} / δ^{syst}, %	δ_1	δ_2	δ_3	δ_4	δ_5	δ_6	δ_7	δ_8	δ_9	δ_{10}	δ_{11}	δ_{12}	δ_{13}	δ_{14}	δ_{15}	δ_{16}	δ_{17}
0.00000 - 0.03361	0.10	-0.34	0.11	-0.08	0.07	1.44	0.35	0.13	0.68	-0.73	-0.68	0.90	-0.19	-0.10	0.02	-0.25	0.80
0.03361 - 0.05106	0.21	0.03	-0.23	-0.06	-0.11	-0.35	0.16	-0.21	0.48	-0.78	-0.71	1.18	-0.63	-0.09	-0.02	-0.04	-0.17
0.05106 - 0.06721	-0.19	0.12	-0.34	-0.02	-0.19	-0.53	0.17	-0.21	0.41	-0.86	-0.78	1.22	-0.86	-0.07	-0.02	-0.05	-0.26
0.06721 - 0.08356	-0.05	0.11	-0.45	0.02	-0.24	-0.49	0.32	0.05	0.43	-0.92	-0.88	1.23	-0.92	-0.06	-0.02	-0.05	-0.09
0.08356 - 0.1000	-0.08	-0.11	-0.48	0.05	-0.23	-0.35	0.45	0.16	0.42	-0.90	-0.96	1.17	-0.98	-0.05	-0.02	-0.05	0.05
0.1000 - 0.1246	-0.07	-0.10	-0.39	0.06	-0.15	-0.21	-0.50	0.15	0.37	-0.94	-1.03	1.11	-0.93	-0.03	-0.02	-0.05	0.07
0.1246 - 0.1535	0.03	0.09	-0.27	0.06	0.10	-0.12	0.46	0.15	0.30	-0.90	-1.10	1.03	-0.88	-0.02	-0.01	-0.05	0.04
0.1535 - 0.1870	-0.09	-0.19	-0.23	0.04	-0.12	-0.05	0.51	-0.13	0.26	-0.94	-1.14	1.13	-0.79	-0.00	-0.01	-0.05	0.01
0.1870 - 0.2277	-0.03	-0.10	-0.20	0.02	-0.24	0.02	0.43	-0.06	0.25	-0.89	-1.19	1.08	-0.74	0.01	-0.01	-0.04	-0.07
0.2277 - 0.2800	-0.06	-0.18	-0.15	0.01	-0.35	0.01	0.22	0.08	0.20	-0.87	-1.26	1.05	-0.77	0.02	-0.01	-0.03	-0.24
0.2800 - 0.3590	-0.06	-0.06	0.19	0.01	-0.36	0.01	0.27	0.12	0.17	-0.81	-1.32	1.03	-0.81	0.03	0.00	-0.01	-0.46
0.3590 - 0.4583	0.08	-0.22	0.57	0.01	-0.31	0.02	0.15	0.06	0.14	-0.72	-1.36	0.98	-0.93	0.04	-0.01	0.02	-0.33
0.4583 - 0.5838	0.10	-0.30	0.76	0.00	-0.26	0.02	-0.17	0.07	0.07	-0.58	-1.38	1.06	-1.25	0.03	-0.14	0.05	1.10
0.5838 - 0.7500	0.11	-0.45	0.85	0.00	0.04	0.03	-0.24	0.12	0.03	0.16	-1.48	1.32	-1.60	0.03	-0.34	0.07	2.82

Table 12

Summary of the systematic uncertainties on the measurement of $\mathcal{R}\mu\mu$ as a function of x_{Bj}. Each column gives the relative change δ_i resulting from a 1σ variation of the corresponding parameter i.

$\sqrt{\hat{s}}$	Bin center	$\sigma_{\mu\mu}/\sigma_{cc} \pm \delta^{stat} \pm \delta^{syst}$ (10^{-3})	δ^{stat}, %	δ^{syst}, %
3.000 - 3.870	3.440	3.620 ± 0.360 ± 0.098	9.93	2.70
3.870 - 4.570	4.213	5.148 ± 0.304 ± 0.138	5.91	2.68
4.570 - 5.250	4.897	5.600 ± 0.238 ± 0.147	4.26	2.63
5.250 - 5.800	5.509	6.041 ± 0.239 ± 0.149	3.95	2.47
5.800 - 6.301	6.035	6.523 ± 0.244 ± 0.152	3.74	2.33
6.301 - 6.818	6.543	6.815 ± 0.239 ± 0.150	3.51	2.19
6.818 - 7.326	7.049	7.190 ± 0.251 ± 0.148	3.49	2.06
7.326 - 7.849	7.567	7.507 ± 0.260 ± 0.148	3.46	1.97
7.849 - 8.407	8.110	7.738 ± 0.264 ± 0.141	3.41	1.82
8.407 - 9.000	8.683	8.187 ± 0.278 ± 0.150	3.40	1.83
9.000 - 9.801	9.375	8.475 ± 0.259 ± 0.145	3.06	1.71
9.801 - 10.74	10.24	8.583 ± 0.261 ± 0.139	3.04	1.62
10.74 - 11.93	11.30	9.142 ± 0.274 ± 0.152	3.00	1.66
11.93 - 14.00	12.82	9.713 ± 0.289 ± 0.184	2.97	1.90
14.00 - 18.00	15.39	10.373 ± 0.435 ± 0.287	4.19	2.76

Table 13
Measured $\mathcal{R}_{\mu\mu}$ as a function of the cernter of mass energy $\sqrt{\hat{s}}$ including both statistical and total systematic uncertainties. The last two columns provide the corresponding relative uncertainties.

$\sqrt{\hat{s}}$ / δ^{syst}, %	δ_1	δ_2	δ_3	δ_4	δ_5	δ_6	δ_7	δ_8	δ_9	δ_{10}	δ_{11}	δ_{12}	δ_{13}	δ_{14}	δ_{15}	δ_{16}	δ_{17}
3.000 - 3.870	0.17	-0.18	0.61	0.05	0.14	-0.45	0.04	0.11	0.36	-0.80	-1.11	0.44	-2.10	0.04	-0.09	-0.01	0.09
3.870 - 4.570	0.14	-0.12	0.40	0.02	-0.21	-0.43	0.03	-0.10	0.40	-0.58	-1.04	1.72	-1.48	0.02	-0.05	-0.03	0.05
4.570 - 5.250	0.14	-0.08	0.25	0.02	-0.33	-0.34	0.01	0.07	0.45	-0.47	-0.99	2.07	-0.97	0.01	-0.02	-0.03	0.02
5.250 - 5.800	-0.06	-0.11	0.11	0.03	-0.35	-0.22	-0.00	-0.03	0.51	-0.41	-0.96	2.03	-0.65	0.00	-0.00	-0.04	0.00
5.800 - 6.301	0.06	-0.08	0.02	0.04	-0.30	0.24	-0.00	-0.03	0.50	-0.40	-0.95	1.93	-0.50	-0.00	0.01	-0.04	-0.01
6.301 - 6.818	-0.06	-0.18	-0.07	0.05	-0.25	0.23	0.01	-0.04	0.51	-0.38	-0.96	1.79	-0.35	-0.01	0.01	-0.04	-0.02
6.818 - 7.326	-0.04	-0.12	-0.09	0.05	-0.22	0.21	0.02	-0.05	0.51	-0.37	-0.97	1.64	-0.28	-0.01	0.02	-0.04	-0.02
7.326 - 7.849	-0.15	-0.09	-0.10	0.04	-0.20	0.21	0.04	-0.04	0.51	-0.31	-1.01	1.54	-0.18	-0.02	0.02	-0.03	-0.03
7.849 - 8.407	0.01	-0.13	-0.11	0.04	-0.18	0.20	0.07	0.06	0.50	-0.37	-1.05	1.30	-0.12	-0.02	0.03	-0.03	-0.03
8.407 - 9.000	-0.12	0.09	-0.14	0.03	-0.17	0.18	0.10	0.06	0.48	-0.37	-1.08	1.30	-0.04	-0.02	0.03	-0.03	-0.03
9.000 - 9.801	0.10	0.08	-0.16	0.02	-0.18	0.14	0.13	0.06	0.48	-0.39	-1.13	1.07	0.03	-0.01	0.04	-0.03	-0.03
9.801 - 10.74	0.09	0.16	-0.19	0.02	-0.21	0.12	0.22	0.05	0.47	-0.34	-1.18	0.83	0.10	-0.02	0.04	-0.03	-0.03
10.74 - 11.93	-0.24	-0.14	-0.22	0.01	-0.25	0.09	0.40	0.03	0.55	-0.36	-1.21	0.68	0.16	-0.02	0.04	-0.04	-0.03
11.93 - 14.00	-0.23	-0.06	-0.30	-0.01	-0.28	0.08	0.87	0.01	0.74	-0.40	-1.23	0.57	0.24	-0.04	0.05	-0.06	-0.02
14.00 - 18.00	0.15	-0.10	-0.46	-0.03	-0.30	0.07	1.96	0.06	1.12	-0.38	-1.23	0.61	0.38	-0.08	0.05	-0.13	0.01

Table 14

Summary of the systematic uncertainties on the measurement of $\mathcal{R}\mu\mu$ as a function of the cernter of mass energy $\sqrt{\hat{s}}$. Each column gives the relative change δ_i resulting from a 1σ variation of the corresponding parameter i.

	$m_c(m_c)$ (GeV)	κ_s
E531+NuTeV+CCFR [22]	1.010 ± 0.095	0.62 ± 0.05
E531+NOMAD	1.058 ± 0.059	0.63 ± 0.04
E531+NOMAD+NuTeV+CCFR	1.070 ± 0.067	0.61 ± 0.02

Table 15
Charm production parameters obtained from different global PDF fits with $\overline{\rm MS}$ running mass [22]. *(NOTE: the table has to be completed since some fits are still running)*

References

[1] S. Alekhin, S. Kulagin, and R. Petti. Determination of Strange Sea Distributions from Neutrino- Nucleon Deep Inelastic Scattering. *Phys. Lett.*, B675:433–440, 2009.

[2] H. Abramowicz et al. Experimental Study of Opposite Sign Dimuons Produced in Neutrino and anti-neutrinos Interactions. *Z. Phys.*, C15:19, 1982.

[3] P. Vilain et al. Leading-order QCD analysis of neutrino induced dimuon events. *Eur. Phys. J.*, C11:19–34, 1999.

[4] P. Astier et al. Neutrino production of opposite sign dimuons in the NOMAD experiment. *Phys. Lett.*, B486:35–48, 2000.

[5] M. Goncharov et al. Precise measurement of dimuon production cross-sections in nu/mu Fe and anti-nu/mu Fe deep inelastic scattering at the Tevatron. *Phys. Rev.*, D64:112006, 2001.

[6] A. O. Bazarko et al. Determination of the strange quark content of the nucleon from a next-to-leading order QCD analysis of neutrino charm production. *Z. Phys.*, C65:189–198, 1995.

[7] A. Kayis-Topaksu et al. Leading order analysis of neutrino induced dimuon events in the CHORUS experiment. *Nucl. Phys.*, B798:1–16, 2008.

[8] N. Ushida et al. Cross-section for neutrino production of charmed particles. *Phys. Lett.*, B206:375–379, 1988.

[9] A. Kayis-Topaksu et al. Measurement of topological muonic branching ratios of charmed hadrons produced in neutrino induced charged- current interactions. *Phys. Lett.*, B626:24–34, 2005.

[10] S. Alekhin, S. A. Kulagin, and R. Petti. Modeling Lepton-Nucleon Inelastic Scattering from High to Low Momentum Transfer. *AIP Conf. Proc.*, 967:215–224, 2007.

[11] S. A. Kulagin and R. Petti. Structure functions for light nuclei. *Phys. Rev.*, C82:054614, 2010.

[12] S. A. Kulagin and R. Petti. Neutrino inelastic scattering off nuclei. *Phys. Rev.*, D76:094023, 2007.

[13] S. A. Kulagin and R. Petti. Global study of nuclear structure functions. *Nucl. Phys.*, A765:126–187, 2006.

[14] Bardin D. Y. Arbuzov, A. B. and L.V. Kalinovskaya. Radiative Corrections to Neutrino Deep Inelastic Scattering Revisited. *JHEP*, 78:506, 2005.

[15] Howard Georgi and H. David Politzer. Freedom at Moderate Energies: Masses in Color Dynamics. *Phys. Rev.*, D14:1829, 1976.

[16] P. D. B. Collins and T. P. Spiller. The Fragmentation of Heavy Quarks. *J. Phys.*, G11:1289, 1985.

[17] C. Peterson, D. Schlatter, I. Schmitt, and Peter M. Zerwas. Scaling Violations in Inclusive e+ e- Annihilation Spectra. *Phys. Rev.*, D27:105, 1983.

[18] N. Ushida et al. Production characteristics of charmed particles in neutrino interactions. *Phys. Lett.*, B206:380–384, 1988.

[19] Tim Bolton. Determining the CKM parameter V(cd) from nu N charm production. 1997.

[20] P. Astier et al. Prediction of neutrino fluxes in the NOMAD experiment. *Nucl. Instrum. Meth.*, A515:800–828, 2003.

[21] C. Amsler et al. [Particle Data Group]. *Phys. Lett.*, B667:1, 2008.

[22] S. Alekhin and S. Moch. Heavy-quark deep-inelastic scattering with a running mass. 2010.